2-1-2016

# Assessing Topside Thermal Solutions for Hot Spot Management of Micro-Scale Electronics

Ryan Shaffer

Ryan Shaffer

*Candidate*

Mechanical Engineering

*Department*

This thesis is approved, and it is acceptable in quality and form for publication:

*Approved by the Thesis Committee:*

Dr. Yu-Lin Shen , Chairperson

Dr. Andrea Mammoli

Dr. Thomas Beechem

# Assessing Topside Thermal Solutions for Hot Spot Management of Micro-Scale Electronics

by

**Ryan Shaffer**

B.S., Mechanical Engineering, University of New Mexico, 2012

THESIS

Submitted in Partial Fulfillment of the
Requirements for the Degree of

Master of Science
Mechanical Engineering

The University of New Mexico

Albuquerque, New Mexico

December, 2015

# Dedication

*I dedicate the time and work devoted to the research presented in this thesis to my family. Their unconditional love and support have been the driving force throughout my life, for which I will always be grateful.*

# Acknowledgments

I would like to extend a special thanks to my mentor Dr. Thomas Beechem. His patience, guidance, encouragement, and example provided an invaluable foundation for both professional and personal growth. Another special thanks goes to Dr. Michael Siegal and Anthony McDonald who supplied additional support and encouragement throughout my research and time at Sandia. I would also like to thank my advisor Dr. Yu-Lin Shen for his time and counsel. Dr. Shen has made my experience as a graduate student both seamless and enjoyable, while offering continuous academic insight and advise. Additionally, I would like to thank Dr. Andrea Mammoli for graciously donating his time as a member on my thesis committee. Last but not least, I would like to thank all of my friends and colleagues. While the path to graduation was a long and challenging one, the struggle was softened by the friendship, joys, and distractions they provided.

# Assessing Topside Thermal Solutions for Hot Spot Management of Micro-Scale Electronics

by

**Ryan Shaffer**

B.S., Mechanical Engineering, University of New Mexico, 2012

M.S., Mechanical Engineering, University of New Mexico, 2015

## Abstract

Thermal limitations are an increasing issue in micro-electronic performance and reliability. This study looks to address a subcategory of the issue, termed "hot spots", which stems from large power densities contained within increasingly smaller electronic components. Topside chip integrated thermal solutions are proposed as an approach for thermal management of these hot spots, where carbon materials are expected to perform exceptionally well. These proposals are assessed via finite element analysis simulations, which are partially verified through electrical thermometry and infrared thermography. The simulations investigate two scenarios: (1) where a single body of material is placed atop the device to spread heat away from the electronic component, effectively cooling it. (2) where said heat-spreader is also in contact with the device package (*i.e.*, thermal ground). The simulations indicate that while scenario 2 is optimal, a thick heat-spreader is of greatest consequence.

A second aspect of the thesis looks into volumetric averaging in infrared thermography measurements. The approach simulates the physics of the temperature

mapping technique in order to highlight the source and severity of the volumetric average based on stack thermal emission and optical analysis. These simulations provide a means of removing the measurement averages via a bottom up approach of comparing the inputed temperature profile to the simulated temperature value. We perform these simulations on FEA model inputs, material stack dimensions, and optical properties, to produce a series of temperatures which show good agreement with the infrared thermography measurement.

# Contents

**List of Figures** **xi**

**List of Tables** **xv**

**1 Introduction** **1**

1.1 Hot Spots in Microelectronics . . . . . 1

1.2 Topside Thermal Solutions . . . . . 2

1.3 Carbon Materials . . . . . 7

1.3.1 Graphene . . . . . 8

1.3.2 HOPG . . . . . 9

1.3.3 Diamond . . . . . 9

1.3.4 Carbon Nano-Tubes . . . . . 10

1.4 Previous Studies . . . . . 11

1.5 Approach . . . . . 13

**2 Device and Model Description** **14**

2.1 Overview of Models . . . . . 14

2.1.1 Control Model . . . . . 14

2.1.2 Topside Heat Spreaders . . . . . 17

2.1.3 Topside Heat Sinks . . . . . 17

2.2 Finite Element Mesh / Boundary Conditions . . . . . 19

2.2.1 Control Model Mesh . . . . . 19

2.2.2 Topside Heat Spreader Mesh . . . . . 21

2.2.3 Topside Heat Sink Mesh . . . . . 22

**3 Control Model Validation** **25**

3.1 Overview . . . . . 25

3.2 Electrical Thermometry . . . . . 26

3.3 Infrared Thermography . . . . . 29

3.4 Results . . . . . 32

**4 Topside Thermal Solution Results** **34**

4.1 Overview . . . . . 34

4.2 Topside Heat Spreader Simulations . . . . . 35

4.3 Topside Heat Sink Simulations . . . . . 37

**5 Simulating Infrared Thermogrphay** **40**

5.1 Simulating Stack Thermal Emission . . . . . 41

5.2 Simulating Infrared Depth Average . . . . . 58

5.3 Simulating Infrared Diffraction . . . . . 60

5.4 IR Simulation on Control Model . . . . . 63

**6 Conclusions and Suggested Future Work** **71**

6.1 Carbon Based Topside Thermal Solutions . . . . . 71

6.2 IR Thermography Simulations . . . . . 72

6.3 Future Work . . . . . 73

# List of Figures


1.1 Illustration of 1-D thermal resistor circuit for a device with, and without a topside thermal solution. By adding a parallel channel, the temperature rise is reduced. . . . . 3

1.2 Approximated 1-D hot-spot temperature reduction vs heat spreader resistance multiplier. . . . . 6

1.3 Illustration of the wide range of thermal conductivities carbon crystalline materials possess. Values are pulled from the references stated in the following sections. . . . . 7

2.1 a.)Optical image, and b.)Cross-section diagram of the control heater device. Inset of (a) shows false color highlighting individual cuboids used in analysis of heater . . . . . 15

2.2 Diagram of the moated and blanket topside heat spreader geometries 17

2.3 Diagram of the topside heat sink configurations integrated into a duel inline package . . . . . 19

2.4 Finite element mesh of the primary control model bodies . . . . . 19

2.5 a.) Refined finite element meshing region, and b.) Resultant control model temperature solution. . . . . 20

2.6 Finite element mesh of the heat spreading bodies . . . . . 21

2.7 Finite element mesh of the topside copper ribbon heat sink . . . . . 22

2.8 Finite element mesh of the topside CNT array heat sink . . . . . 23

3.1 a.) Measured device TCR data, and b.) Subsequent TCR temperature of powered device shown in Figure 3.3a. . . . . 27

3.2 a.) Measurement of Resistance, and b.) Resistivity of the micro-heater for isothermal calibration . . . . . 28

3.3 a.) IR thermography measurement map, ans b.) FEA control model simulation, both with a $90^oC$ back plate and a total power dissipation of 0.5 watts . . . . . 32

3.4 (a) Nominal heater temperatures obtained *via* each thermal characterization technique plotted as a function of power dissipation, and (b) difference in peak temperatures over the dashed lines in Figure 3.3 plotted as a function of measured IR resolution. . . . . 32

4.1 Top-side heat spreader simulation results . . . . . 35

4.2 Cooling capability of a.) graphene and b.) graphite as a function of layer thickness. . . . . 36

4.3 a.) 2-way stand-alone heat-spreader simulation results, b.) 3-way copper ribbon heat-sink simulation results, and c.) 3-way CNT array heat-sink simulation results . . . . . 37

5.1 a.) Temperature Dependent Black-Body Thermal Emission, b.) over QFI MWIR sensing range. . . . . 41

5.2 a.) Diagram of light transfer in thin film stack, and b.) Depiction of the implication in IR thermography. . . . . 47

5.3 Diagram of the depth dependent stack transmission parameters and approach. . . . . 52

5.4 Simulated vs analytical emissivity of a.) Platinum, and b.) $SiO_2$ for varying body thickness in air. . . . . 56

5.5 Diagram depicting an IR thermography procedure using Eq 5.8 and 5.33 . . . . . 59

5.6 a.) Measured radiance profile over a precision resolution target and its spacial derivative, and b.) Lorentzian fit to the derivative data. . 61

5.7 Depth averaged Si-microheater line temperature with example diffraction limited pixel temperature (top) and the corresponding spacial Lorentzian pixel weighting functions (bottom). . . . . 62

5.8 b.) FEA surface temperature vs measured IR temperature over the line depicted in (a). . . . . 64

5.9 a.) Silicon substrate cross-sectional temperature map, and b.) Extracted line temperature profile with scaled heater and oxide profiles for depth average. . . . . 65

5.10 b.) FEA surface temperature with depth average vs measured IR temperature, over the line depicted in (b). . . . . 67

5.11 Measured a.) full width half max parameter $G$, and b.) pixel resolution, for various objective magnifications on an MWIR QFI Infrascope. 68

5.12 b.) FEA surface temperature with full simulation vs measured IR temperature, over the line depicted in (a). . . . . 69

5.13 FEA surface temperature with full simulation vs measured IR temperature for a power input of 0.5 Watts at various objective magnifications. . . . . 69

5.14 FEA surface temperature with full simulation vs measured IR temperature for a power input of 0.3 Watts at various objective magnifications. . . . . 70

5.15 FEA surface temperature with full simulation vs measured IR temperature for a power input of 0.15 Watts at various objective magnifications. . . . . 70

# List of Tables

2.1 Thermal Properties Utilized in Simulation @ $T > 25^oC$ . . . . . 16

5.1 Material Stack Optical Properties . . . . . 65

# Chapter 1

# Introduction

## 1.1 Hot Spots in Microelectronics

As integrated circuits become smaller through advancements in fabrication capabilities and technologies, power densities in electronic components are reaching levels that induce extreme temperatures. While these temperature rises (*i.e.*hot-spots) are not representative of the whole system, they create bottle necks in overall system performance and reliability, thus limiting the potential of the system. In response, we pursue a solution that can be integrated into established designs to provide an inexpensive and versatile reduction of operating temperature. Specifically, topside thermal solutions are considered here for their ease of integration, close proximity to thermally active region, and largely untapped potential.

To asses these solutions, it is necessary to first characterize these hot spots in order to identify the severity of the issue, as well as validate the potential solution. Infrared thermography is a widely used tool capable of quickly obtaining temperature maps based on Planck's equation of thermal emission. However depending on the optical properties of the material stack being measured, as well as the diffraction limitations

of the measurement, these temperature maps may contain volumetric errors that can lead to inaccurate conclusions. Predicting and quantifying these averaging effects allows for greater insight into the measurement as well as better comparisons to models, therefor greatly increasing its utility in microelectronic applications.

The work presented in this thesis addresses these issues, with a strong focus on carbon based topside thermal solutions for the management of hot spots in micro-scale electronics. First, carbon based top-side thermal solutions are investigated through a numerical study to identify an ideal material constituent and architecture. Subsequently, errors induced by volumetric averaging in IR-thermography are assessed to both explain discrepancies in the model validation, and to provide insight into errors implicit with the use of this popular technique. To motivate efforts, the remainder of this chapter highlights the utility of top-side thermal solutions.

## 1.2 Topside Thermal Solutions

In traditional microelectronic packaging, all generated heat must travel downward through the substrate to thermal ground (i.e., the heat sink package), dissipating at a rate proportional to the thermal resistance of the materials required for device operation. Since the pathway to thermal ground is typically accompanied by layers and interfaces possessing large thermal resistance, highly localized heat dissipation can manifest to produce large temperature rises near regions of heat production. In order to reduce the magnitude of this temperature rise, one could either change the materials and dimensions used in the device stack itself, or simply introduce a new path for heat to travel. Here, the latter option is pursued through investigation of a top-side thermal solution. A top-side solution effectively splits generated heat between the downward path through the substrate, and through an upward/lateral path of a material of choice. Choosing a material with a high thermal conductivity

will move heat more efficiently, resulting in a smaller temperature rise in thermally active regions. This cooling effect is governed by Fourier's law of heat conduction, meaning that the total heat flux away from active regions will be a function of thermal conductivity, spreader thickness, and imposed temperature differentials, thus defining the system we wish to balance.

To illustrate the benefits of a topside thermal solution, we make use of a 1-D thermal resistor diagram shown in Figure 1.1 below.

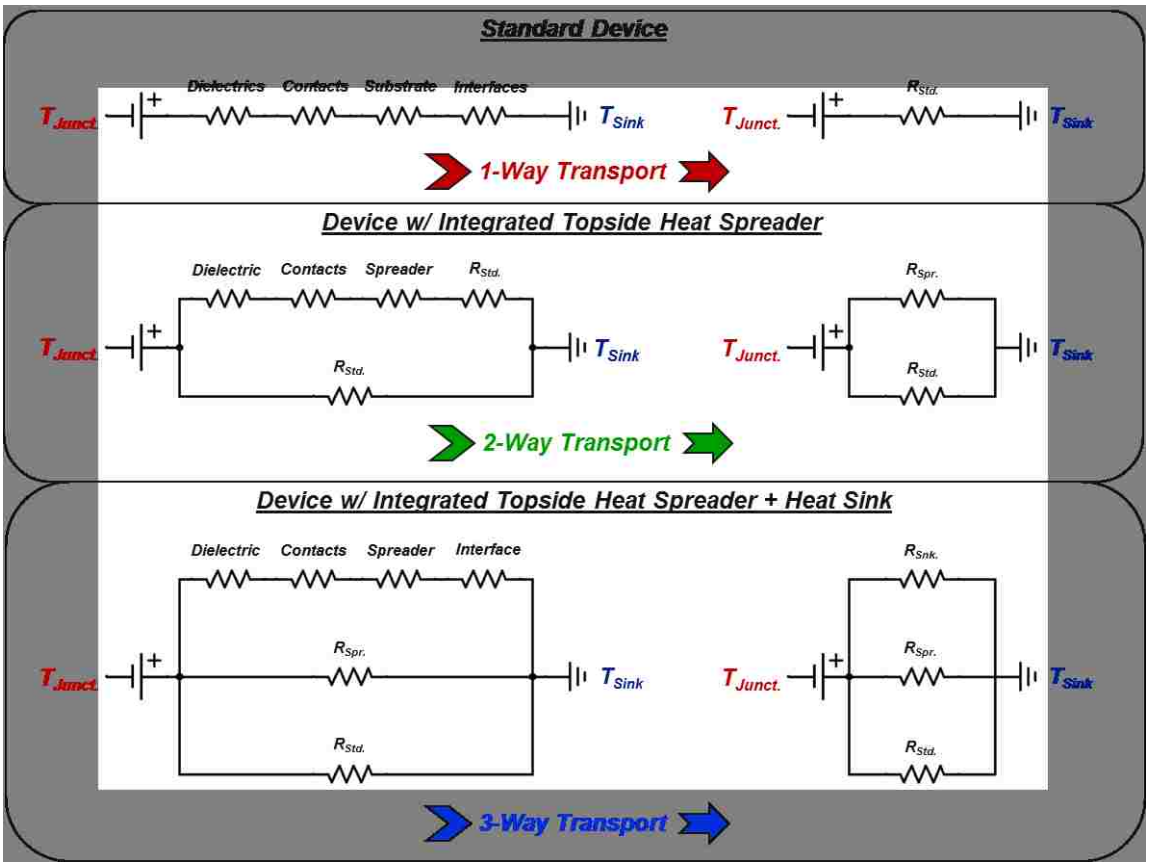


Figure 1.1: Illustration of 1-D thermal resistor circuit for a device with, and without a topside thermal solution. By adding a parallel channel, the temperature rise is reduced.

As shown, each thermal circuit is composed of a hot-spot to room temperature

differential ($\Delta T = T_{Junct.} - T_{Sink}$) which is separated by a series of the thermal resistances that makes up the device geometry. The magnitude of this temperature difference is related to the effective thermal resistance of the circuit and the heat flux, $\dot{q}$, flowing through it via Eq 1.1.

$$\Delta T = \dot{q} \cdot R_{eq} \tag{1.1}$$

In a standard architecture generated heat has but one path to travel, thus producing the equivalent resistance in Eq 1.2.

$$R_{eq1} = R_{Std.} \tag{1.2}$$

where $R_{std.}$ is a resistance of the substrate stack consisting of thermal resistance associated with the active layer and substrate, along with any interfaces and contacts separating the junction from thermal ground. To reduce $R_{eq}$, a top-side solution can be utilized. The simplest form is a heat spreader that functionally expands the area through which heat travels. Practically, a heat spreader consists of a material layer possessing high thermal conductivity that lays atop the junction area. From a thermal circuit perspective, the heat spreader turns the standard series circuit into a parallel circuit, therefore reducing the total resistance from Eq 1.2 to Eq 1.3. (See Figure 1.1)

$$R_{eq2} = \left( \frac{1}{R_{Spr.}} + \frac{1}{R_{Std.}} \right)^{-1} \tag{1.3}$$

where $R_{Spr.}$ is the resistance of the additional thermal pathways opened up by the spreader. While a heat spreader does open up an additional pathway to transport,

its utility is mitigated since heat after being "spread" must still travel through the standard device stack. If instead the spreader itself was directly connected to the thermal ground, the total resistance of the new pathway could be greatly reduced. Functionally, such sinking may be realized by connecting the top of the spreader to the package by using a wire bond as a thermal conduit. From a thermal circuit perspective, the thermal sink can be viewed as an additional parallel path having an effective resistance defined by Eq 1.4.

$$R_{eq3} = \left( \frac{1}{R_{Snk.}} + \frac{1}{R_{Spr.}} + \frac{1}{R_{Std.}} \right)^{-1} \tag{1.4}$$

where $R_{Std.}$ is the sum of the resistances in the standard path, $R_{Spr.}$ is the sum of the resistances through the topside heat spreader path, and $R_{Snk.}$ is the sum of the resistances through the topside heat sink path (as diagrammed in Figure 1.1).

Using the discussed variations in equivalent resistance, we now seek to assess how the temperature rise compares for each of the architectures using Eq 1.1. To facilitate, the sink and spreading resistance —$R_{Snk.}$ and $R_{Spr.}$, respectively —are normalized relative to the standard resistance $R_{Std.}$. Since the heat spreader path is equal to the standard path plus the resistance of the spreader materials $R_{Spr.} > R_{Std.}$. We can therefore think of the heat spreader as $R_{Spr.}/R_{Std.}$, which when equal to 1, means a heat spreader resistance of 0. It follows that $R_{Snk.}$ can also be represented by this ratio, as its resistance will scale with spreader resistance. Since we can expect $R_{Snk.} < R_{Std.}$ owing to less material of higher thermal conductivities, the simplifying assumption that $R_{Snk.} = \frac{R_{Spr.}}{2}$ is both conservative and allows us to write $R_{Snk.}$ as function of $R_{Srp.}$. With these assumptions, the equivalent resistances for each of the architectures can be written as a ratio of the thermal solutions resistance relative to that of the standard material stack. Using this ratio, the utility of the thermal solution can thus be probed using Eq 1.1 together with Equations 1.2, 1.3,

and 1.4. By normalizing the thermal solution's temperature rise relative to that of the standard, a percent reduction in the temperature rise is plotted as a function of $R_{Spr.}/R_{Std.}$ as shown in Figure 1.2 below.

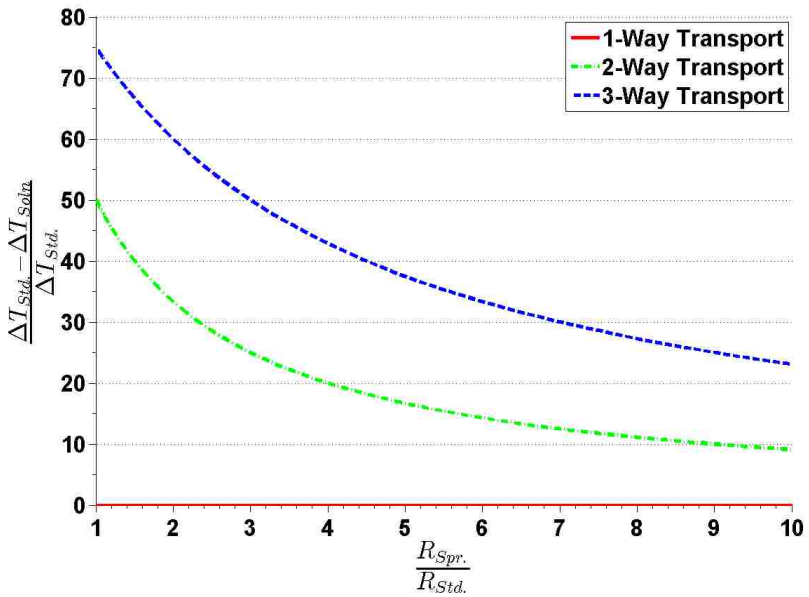


Figure 1.2: Approximated 1-D hot-spot temperature reduction vs heat spreader resistance multiplier.

From Figure 1.2, it is evident that even if the thermal solution has a comparatively high thermal resistance, significant reductions in operating temperature are achievable. Specifically, even if the top-side thermal sink (3-way transport) has a total thermal resistance 5x that of the standard stack, a 35% reduction in the device's temperature rise is achievable. For this reason, we pursue whether such a path could feasibly be realized. To this end, FEA analysis is utilized, as the 1D resistor method is meant only as a rough "back of the envelope" calculation, since temperature dependent properties and 3D effects will undoubtedly influence quantitative results.

A final point to be made about topside thermal solutions is the need for appro-

priate electrical insulation. Since the topside of a device is typically occupied by electrical contacts, applying an electrical conductor across them will short out the chip. This can be overcome by first applying a dielectric over the surface of the device, however since dielectrics typically have poor thermal conductivities, doing so could severely limit the performance of the solution. The ideal material for a topside thermal solution is therefore one with a high thermal conductivity, high electrical insulation, high temperature stabilities, and a flexible nature.

## 1.3 Carbon Materials

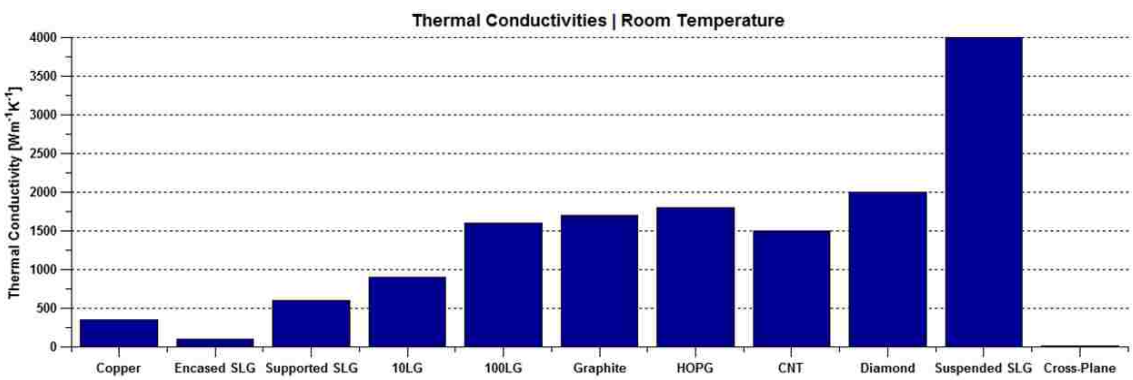


Figure 1.3: Illustration of the wide range of thermal conductivities carbon crystalline materials possess. Values are pulled from the references stated in the following sections.

Carbon materials are an excellent candidate for thermal management applications due to their high thermal diffusivity/conductivities, high temperature stabilities, strong molecular bonds, and in some cases forgiving interfaces. Carbon can naturally organize itself into numerous geometrical structures, each possessing unique properties. Here we focus on their thermal properties with the goal of predicting their usefulness in a practical environment as a top-side thermal solution using Fourier based FEA simulations. To do this, we must first understand and quantify

how these thermal properties vary between each form as it relates to the device geometries in which they will be employed. With the exception of diamond, all of the carbon materials simulated are geometrical derivatives of graphene, therefore we will start there. Figure 1.3 provides a comparison of the reported thermal conductivities of various allotropes of carbon.

### 1.3.1 Graphene

Graphene is a two-dimensional (2D) material composed of carbon atoms arranged in a periodic hexagonal structure. Each carbon atom is attracted to its nearest neighbors via strong covalent $sp^2$ bonds, which are among the strongest and stiffest bonds in nature, giving rise to the high in-plane thermal conductivity of graphene reported to be in excess of 2000 W/mK [1]. In contrast, graphene interacts with its surroundings through weak Van Der Waals forces, resulting in an out of plane thermal conductivity up to 3 orders of magnitude lower than that of the in-plane direction [2]. Despite this relatively weak out of plane coupling, graphene and other $sp^2$ carbons can have their in-plane properties significantly influenced by the surrounding materials. In monolayer graphene that is encased by other materials, for example, phonon scattering at interfaces can reduce the in-plane thermal conductivity by several orders of magnitude [3]. With the stacking of additional layers however, scattering at adjacent bodies becomes less influential to the inner layers, and the stack begins acting as a single low impedance material known as graphite [2, 3]. These scattering mechanisms result in an effective thermal conductivity of graphene that ranges from 3000 W/mK [1], to less than 100 W/mK [3]. From the perspective of a thermal solution, these variations are of profound consequence. Coupled with the fact that they are commensurate with the number of layers and thus the conductance of the system, it remains unclear whether graphene offers any advantage relative to graphite or more traditional cooling materials like copper or diamond. Assessing

these trade-offs is a primary objective of this thesis.

### 1.3.2 HOPG

Highly ordered pyrolytic graphite (HOPG) consists of oriented planes of graphene, stacked so that the center of each hexagonal carbon ring is aligned with a carbon atom from the layers above and below (*i.e.*, Bernal stacking). This stacking orientation reduces phonon scattering mechanisms by optimizing molecular spacings to allow each carbon atom to vibrate with minimal neighboring interference. As a result, HOPG has a room temperature in-plane thermal conductivity approaching 2000 W/mK [3], it has a flexible lattice for even contact with uneven neighboring structures, and can be grown to a desired thickness for adjustable thermal conductance. The downside of using HOPG as a thermal solution is that its out of plane thermal conductivity derives from weak Van Der Waals forces, resulting in less than 10 W/mK [3]. The corresponding low out of plane thermal conductance might prevent any significant amount of heat from entering the upper layers, thus limiting its usefulness.

### 1.3.3 Diamond

Diamond is a unique material popularly known for its incredible strength and desirable optical properties. The diamond crystal is composed of 8 carbon atoms, each sharing a strong $sp^3$ covalent bond with four neighboring atoms, which arrange themselves into a structure appropriately called the diamond cubic crystal structure. The resultant 3D material is lightweight, rigid, isotropic, and posses a thermal conductivity on the order of 2000 W/mK [4]. The practical challenge with diamond is ensuring even cohesion with thermally active regions, as diamond is very stiff and thus not compliant when in intimate contact with other materials. Therefore, while

diamond is the ideal material from a thermal perspective, from a mechanical perspective it is inferior to graphene/graphite, which are more flexible to uneven surfaces and forgiving to strain.

### 1.3.4 Carbon Nano-Tubes

A carbon nanotube (CNT) can be visualized as a single graphene sheet rolled into a cylinder and capped with $C_{60}$ fullerene hemispheres. Their diameters are on the order of nanometers but can span microns in length. They are extremely strong and stiff axially, relatively ductile laterally, and possess excellent electrical and thermal properties. For these reasons CNTs have received much attention for applications in electronic devices [5], as well as for thermal solutions [6]. Here, we examine their utility to passively cool electronics by acting as an efficient thermal interface material (TIM) between a topside heat spreader and the ceiling of a device package. In this application, heat enters a topside heat spreader as previously discussed, however instead of spreading out and redirecting back through the substrate, the heat is removed from the top of heat spreader directly into the heat sink package through the CNTs. This configuration is represented by $R_{Snk.}$ in figure 1.1 and would provide a second option to the heat spreader path of significantly less resistance owing to a shorter distance to ground, higher thermal conductivities, as well as low carbon-carbon contact resistances. However to facilitate this application, fabrication of a CNT array that is planarized, aligned, and untangled is necessary in order to maintain each nanotube's exceptional axial thermal conductivity of greater than 1500 W/mK [7], as well as ensure good even contact with the materials that it interfaces. Siegal *et al.* has developed a technique to grow such an array by fabricating an anodized aluminum-oxide nanoporous template to seed the nanotube growth, control their geometries, and planarize the final array [8].

## 1.4 Previous Studies

Graphene has previoiusly been reported to be an effective heat spreader for microelectronic applications via both experimentation and simulation [9–14]. The following summarizes a few of these studies in order to provide the context by which the current study was motivated.

Balandin *et al.* investigated a seven finger silicon-on-insulator field effect transistor using commercial FEA software [9]. In the models, each transistor finger is approximated as a rectangular heat generating channel separated from one another by 10 $\mu$m of silicon. This transistor array sits on a 100nm layer of $SiO_2$, which is separated from the silicon substrate by a graphene heat spreading layer. Both the back side of the silicon substrate and the sides of the graphene heat spreader are connected to a heat sink (*i.e.*, constant temperature). The study compares the maximum temperate of the device with and without a heat spreader for a varying graphene thickness and thermal conductivity. Simulations were performed for an encased graphene stack of 1 to 100 layers with an assigned isometric thermal conductivity of 1000-5000 W/mK, resulting in a maximum temperature reduction ranging from 15-20%.

Balandin *et al.* also examined graphene's cooling abilities via an experimental study [10]. In this study, an AlGaN/GaN on SiC HEMT was characterized through current-voltage analysis, as well as a Raman thermometry measurement over the anticipated thermal dissipation region between the gate and drain electrodes. A few layers of graphene were then applied to the top side of the device, draping over the drain electrode and connecting to a large chunk of graphite a few microns away. When the device was taken to the same power levels as before, the probed Raman temperature rise had dropped by approximately 20%. It was also observed that more drain current was received for the same source-drain and gate voltages, which was

attributed to an improved thermal saturation current density induced by graphene heat removal. In addition to the measurements, the device was also modeled using FEA simulations. The control model was first validated to the Raman thermometry results of the HEMT without a heat spreader. A graphene to graphite topside solution was then added to the model according to the experimental setup, and an isometric thermal conductivity of 2000 W/mK was assigned to the graphene stack approximated to be ten layers thick. The simulations predicted a 15% reduction in the temperature rise attributed to the graphene heat spreader, and a 6% temperate rise reduction using a heat spreader thermal conductivity typical of a metal.

Liu *et al.* performed a similar experiment as Balandin's group, however instead of using a prefabricated complex transistor device, they fabricated a simple $SiO_2$ passivated platinum line heater with an $SiO_2$ substrate to both supply heat and probe temperature [11]. After characterizing the devices relationship between temperature and electrical resistance in a furnace, the device was powered to various levels and electrical temperatures were calculated and recorded. A single layer of graphene was then deposited onto the top of the device covering the entire heater region, and just as before, the device was powered and probed. The measurements concluded that by adding the topside graphene heat spreader, the device's electrical temperature was reduced by approximately 11%. It is interesting to note that when adding additional layers of graphene, the measured temperature reduction dropped to about 7%. This is unexpected as additional layers should increase both graphene's thermal conductivity, as well as the heat spreaders channel size, both of which should contribute to a larger cooling effect.

Taken together, the underlying theme in much of the literature is that single and few layer graphene will provide enhanced thermal cooling solutions owing to its extraordinary intrinsic thermal conductivity. However, it has been well documented that when graphene makes contact with other materials —for example with a mate-

rial we wish to spread heat from —its thermal conductivity degrades to a value on the order of a good metal [15]. Accounting for this degradation along with the incredibly small cross sectional area of graphene brings into question its practical utility as a heat spreader. While stacks of graphene are less susceptible to these degradations, the through plane thermal conductivity remains on the order of 5 W/mK, bringing further question to its utility. These questions reflect points of deficiency in much of the previous analysis and requires further attention. The FEA simulations presented in this thesis are aimed at examining these questions by comparing the answers to more traditional material solutions in various topside integrated configurations.

## 1.5 Approach

To investigate these questions, a simple metal line heater device was designed with a size and shape to produce localized heating on the scale of a typical microelectronic device. The device was then modeled and validated through electrical and IR thermography measurements (Chapters 2 and 3). Beyond validation of the models, an in-depth analysis of the IR-thermography physics is provided to highlight errors implicit with the technique. This work is presented in Chapter 5. Once the control model was deemed valid, various topside thermal solutions were introduced into the model to asses how each one influences hot-spot magnitudes (Chapters 2 and 4). These variations include scenarios where the heater must remain uncovered, where the heater is completely buried, where a large area of the spreader is attached to the package by an array of CNTs, and where the spreader is attached to the package by copper bonding ribbon near the hot-spot. All scenarios were investigated utilizing a spreader material of graphene, multi-layer graphene, HOPG, diamond, and copper, with assigned temperature dependent thermal conductivities of the values and characteristics previously described.

# Chapter 2

# Device and Model Description

## 2.1 Overview of Models

### 2.1.1 Control Model

A metal-line microheater was fabricated using standard photolithographic processes to dissipate heat within a region of comparable size to many microelectronics. Being composed of a metal stack consisting of a 10nm adhesion layer of titanium (Ti) beneath 100nm of platinum (Pt), the heater not only serves as a heat source but also as a resistance thermometer. The device rests on a substrate of slightly n-doped silicon (535$\mu$m, 5-10 $\Omega - cm$) capped with 300nm of thermal oxide.

Steady state predictions of the temperature field produced by the heater were obtained using ANSYS thermal analysis software. Since heat generation is not uniform owing to the varying width of the heater line, the heater is modeled as a series of rectangular cuboids. Each cuboid volumetrically generates heat at a rate of $q_i''' = I^2\rho/A_{c,i}^2$ where $q_i'''$ is the heat generation within segment $i$ having a cross sectional area of $A_{c,i}$, $I$ is the measured current through the heater, and $\rho$ is the

resistivity of the platinum within which 98% of the heat is expected to be dissipated. Geometrically, each heater segment is modeled as a two-dimensional body to reduce difficulties in meshing that can arise owing to the large aspect ratio. In a similar fashion, thermal resistance offered by the thin titanium and $SiO_2$ layers are included as a single boundary resistance whose magnitude is determined by the resistances to conduction through each layer and at their boundaries [16–19]. The back of the silicon substrate is constrained at $T_o = 23°C$ while other surfaces are presumed to be adiabatic, as estimations indicate less than 3% total heat loss *via* convection and radiation. Meshes were refined until the solution changed by less than 1%. Properties employed within the model are provided in Table 2.1. Diagrams of the control device can be found in Figure 2.1.

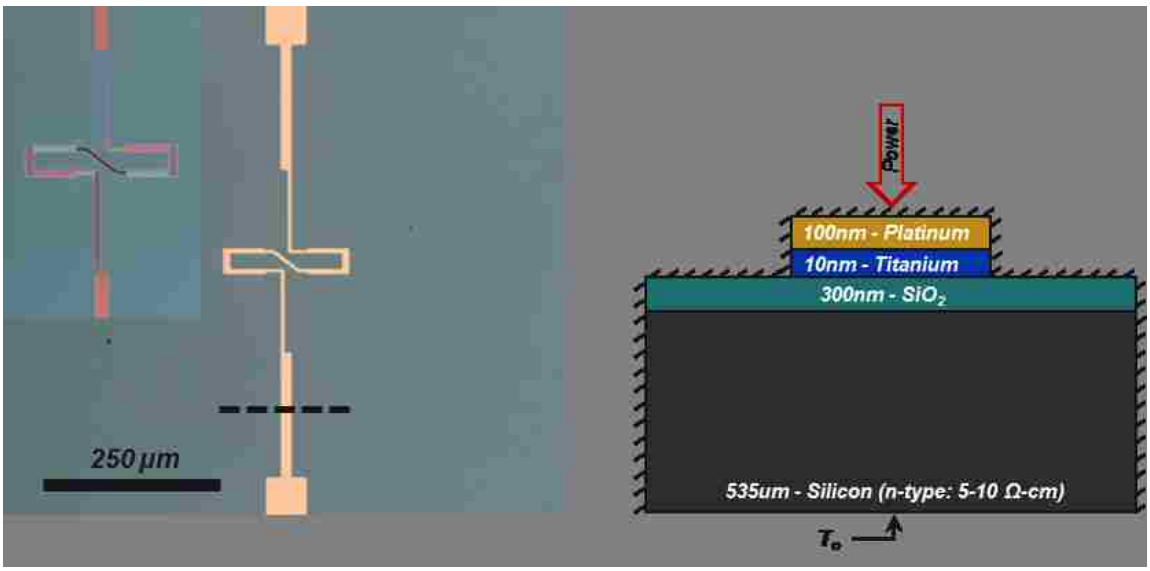


Figure 2.1: a.)Optical image, and b.)Cross-section diagram of the control heater device. Inset of (a) shows false color highlighting individual cuboids used in analysis of heater

Once the control model was developed, top-side thermal solutions composed of graphene (1 to 1000+ layers), graphite, diamond, and copper were each integrated into the model and compared as to their ability to provide an additional thermal

Table 2.1: Thermal Properties Utilized in Simulation @ $T > 25^oC$

| Material | k, W/mK | $h_{1,2}$, $MW/m^2K$ |
|---|---|---|
| *Silicon* | $148(\frac{T}{300})^{-1.3}$ [15] | $h_{Si/SiO_2}$=1000 [17, 21] |
| $SiO_2$ | 1.5 [15] | $h_{SiO_2/Ti}$=20 [16] |
| $SiNx$ | 1 [15] | $h_{SiNx/Cu}$= 25 |
| *Titanium* | 20[15] | $h_{Ti/Pt}$=1000 [22] |
| *Platinum* | $13e^{(-5\times10^{-3}T)} + 64e^{(2\times10^{-4}T)}$ [23] | $h_{Pt/SiNx}$= 25 |
| *Copper* | 380 [15] | $h_{Cu/SLG}$= 100 [19] |
| *Cobalt* | 80 [23] | |
| *HOPG* | $1835(\frac{T}{300})^{-1.203}$ [2] | $h_{HOPG/SiO_2}$= 85 [16] |
| *Graphene* | $-5.524e14 * T^{-5.342} + 594.5$ [20] | $h_{SLG/SiO_2}$= 85 [16] |
| *10 Layer Graphene* | $940(\frac{T}{300})^{-1.203}$ [2, 3] | $h_{MLG/SiO_2}$= 85 [16] |
| *100 Layer Graphene* | $1739(\frac{T}{300})^{-1.204}$ [2, 3] | $h_{MLG/SiO_2}$= 85 [16] |
| *MLG Out of Plane* | $5.796(\frac{T}{300})^{-1.132}$ [2] | $h_{MLG/SiO_2}$= 85 [16] |
| *CNT* | 1500 [7] | $h_{CNT/MLG}$= 1000 [18] |
| *Diamond* | 2000 [4] | |

dissipation pathway. In these simulations, temperature dependent thermal conductivities of single and multi-layer graphene were obtained by normalizing values of thickness dependent thermal conductivities at room temperature [3, 20], to the temperature dependent thermal conductivity profile of graphite [2]. The thermal solution took two different forms. First, the solution comprised only a heat spreading element composed of the material of interest (i.e., graphene, diamond, etc.). Second, the thermal spreading element was connected to a top-side heat sink that allows for heat removal to entirely bypass the device substrate and pass directly into the device package (i.e., the thermal ground). Capability is assessed via a comparison of the maximum temperature with and without the top-side materials.

### 2.1.2 Topside Heat Spreaders

Top-side heat spreaders were introduced into the control model in two configurations, which will be referred to as moated and blanket. The moated configuration has the spreader placed in-plane with the heater and held at a small and constant distance away. The blanket configuration buries the platinum heater under a 20nm layer of silicon nitride and places the spreader atop the nitride over the entirety of the device. Diagrams of these model variations can be found in Figure 2.2. From an application perspective, the moated design corresponds to a situation in which the thermal spreader is placed in a region of open real-estate close, but away, from the active region of a device, whereas the blanket configuration corresponds to an implementation where the spreader is placed directly atop the active region.

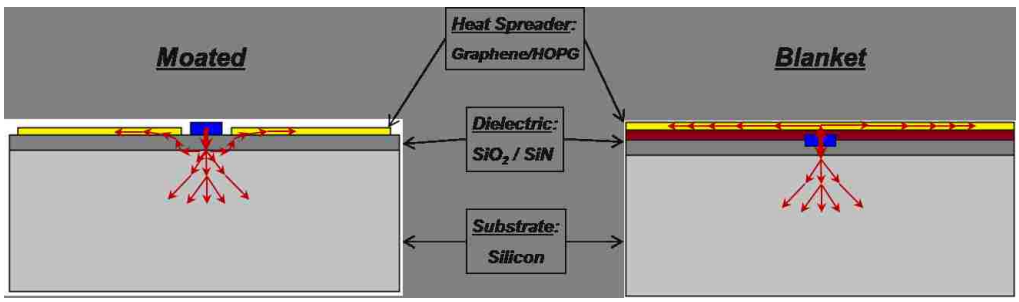


Figure 2.2: Diagram of the moated and blanket topside heat spreader geometries

### 2.1.3 Topside Heat Sinks

In total, the integrated top-side solution has two elements; a heat spreader, and a second element whose purpose is to transport heat out of the spreader and to the thermal ground. Ideally, this second element would have a high thermal conductivity as well as a low thermal boundary conductance between itself and both carbon as well as the metal package. We consider two different scenarios. The first consists of a ribbon bond of copper owing to the material's high thermal conductivity,

low thermal boundary conductance to metal, along with an established ability to be manufactured. Second, we consider carbon nanotubes owing to the possibility of their extreme thermal conductivity (See Figure 1.3) and low thermal boundary conductance to carbon based heat spreaders. Aside from their thermal properties, the ribbon bond configuration has the advantage of simplicity; while the CNT array offers a larger contact area to the spreader, and a shorter path to the package. These factors, along with how well each sink complements each spreader configuration, will determine overall cooling performance.

To illustrate these configurations, the heat spreading model geometries were integrated into a generic dual in-line package as shown in Figure 2.3a. A total of four scenarios were modeled and are described as follows: Figure 2.3b depicts the moated geometry with commercially available 500$\mu$m x 50$\mu$m copper ribbon connecting a region of the heat spreader near the heat source to the package with a ribbon length equal to 8mm. The ribbon is placed on both sides of the heater. Figure 2.3c depicts the moated geometry with a 1$\mu$m thick CNT array contacting a 1mm x 1mm area of the heat spreader on both sides of the heater. The CNT array is assumed to be infinitely dense (i.e., a filling fraction of 1) and grown out of 1um of cobalt which is attached to the aluminum package. Figure 2.3d depicts the blanket geometry with copper ribbon connecting a region of the heat spreader directly over the heat source to the package with a ribbon length equal to 8mm. Figure 2.3e depicts the blanket geometry with a 1$\mu$m thick CNT array contacting a 1mm x 1mm area of the heat spreader directly over the heat source.

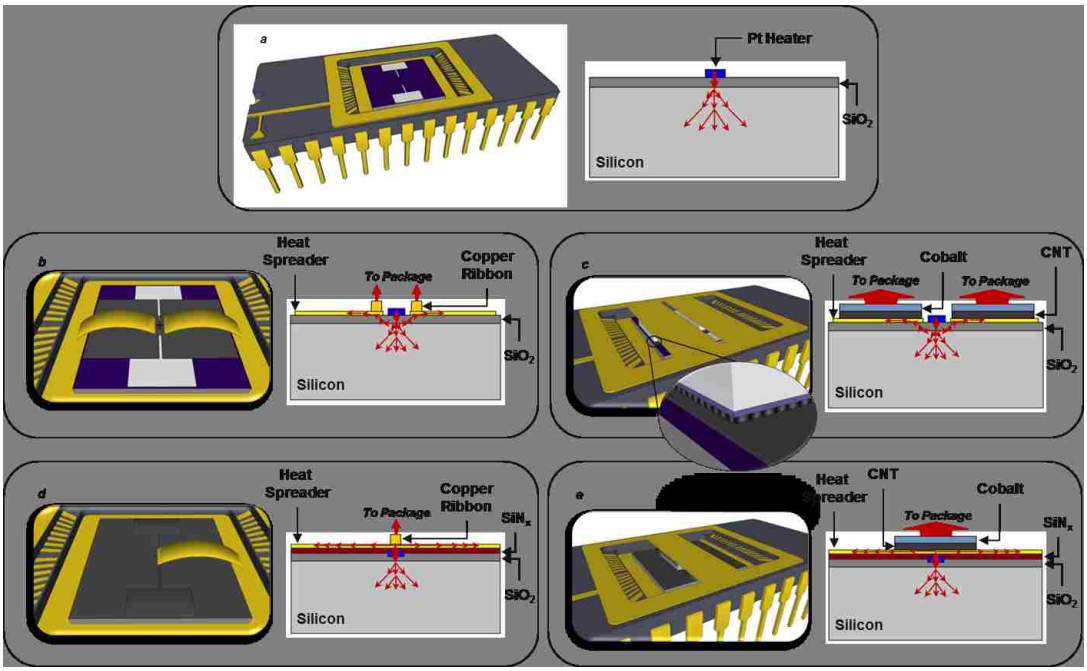


Figure 2.3: Diagram of the topside heat sink configurations integrated into a duel inline package

## 2.2 Finite Element Mesh / Boundary Conditions

### 2.2.1 Control Model Mesh

Figure 2.4 depicts the control model's volumetric mesh. Throughout the model, quadrilateral elements are enforced onto body surfaces of increasing refinement with

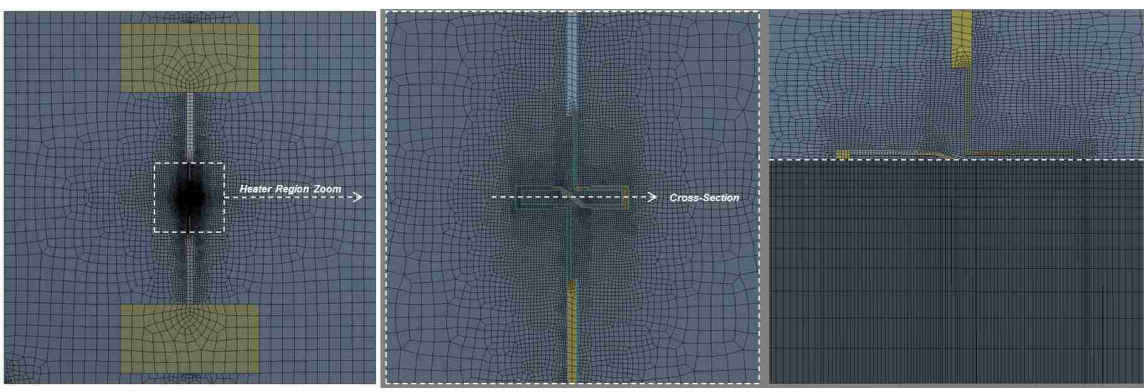


Figure 2.4: Finite element mesh of the primary control model bodies

proximity to regions of heat dissipation. Figure 2.4b shows the region of most concentrated heat dissipation, in which the heater's fine mesh is mirrored onto the silicon surface beneath it. From there, the silicon in-plane mesh grows in size at a controlled rate to a defined maximum element width. That surface mesh is defined to be constant throughout the thickness of the silicon with through thickness nodes set at intervals with a growing rate from the surface, as shown in Figure 2.4c. In this way, the smallest elements are located near the center of the heater and grow larger in all directions. As discussed previously, each heater cuboid is assigned internal heat generation so that it produces a percentage of the total inputed power proportional to its relative contribution of electrical resistance. The back of the silicon is held at a constant temperature of $23^oC$, and the top/sides of the model are assumed adiabatic. The model domain is increased until the adiabatic sides no longer influence the thermal solution.

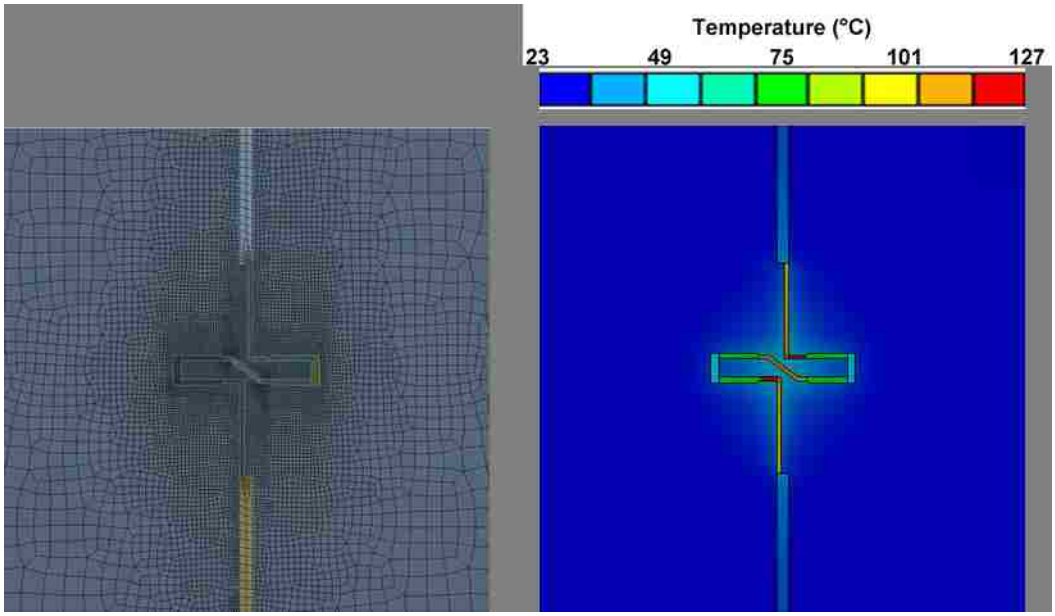


Figure 2.5: a.) Refined finite element meshing region, and b.) Resultant control model temperature solution.

Figure 2.5 depicts the FEA simulated temperature map of the control model for

a total input power of 1 Watt. Regions of largest temperature rise are located near the center of the heater, in the bodies with smallest cross-section area. If a topside thermal solution is introduced into the model with close enough proximity to these temperature spikes, we should expect a decrease in heat densities via more efficient heat removal, resulting in reduction of maximum temperature. An ideal topside thermal solution would make direct contact with the heater hot-spots, maximizing thermal solution temperature differential and thus heat removal. However there are instances when device functionality prohibits this, thus limiting the thermal solution to a finite proximity. Both scenarios are considered and simulated through the blanket and moated heat spreader.

### 2.2.2 Topside Heat Spreader Mesh

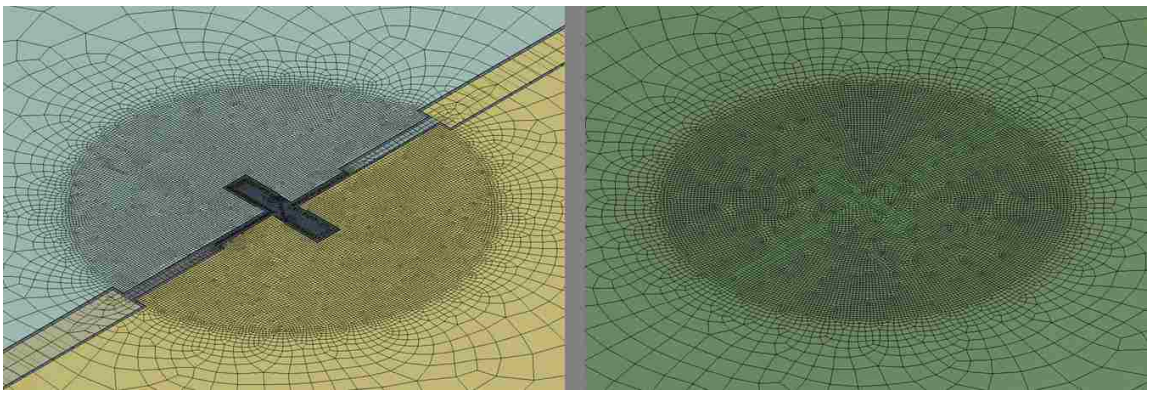

Figure 2.6: Finite element mesh of the heat spreading bodies

Figure 2.6 depicts the mesh implemented for each topside heat spreader configuration. In both configurations, the spreader is assigned the same meshing style and sizing as the control model, however the refinement zones are defined by a concentric circle with the heater center, rather than rectangles mirroring the heater shape. The Moated configuration, shown in Figure 2.6a, is composed of two heat spreaders placed on top of the silicon body each maintaining a close proximity to the line

heater. Meanwhile the Blanket configuration, shown in Figure 2.6b, is composed of a single heat spreading body contacting the top surface of the entire control model. Owing to their thinness, the SiNx and $SiO_2$ layers are incorporated as equivalent interface resistances. The assigned resistance accounts for both resistance to heat transfer through the layers and the respective Kapitza conductances. When the heat spreader is modeled to represent single and few layer graphene, the body is defined to be a two dimensional shell, much like the heater. This allows for a proper mesh without dealing with the extreme aspect ratios a $3\mathring{A}$ thick layer induces. This two dimensional assumption is valid in these instances as we expect a negligible temperature gradient to manifest over a few atomic layers. Bodies thicker than $300nm$ are modeled as three dimensional.

### 2.2.3 Topside Heat Sink Mesh

#### Copper Ribbon

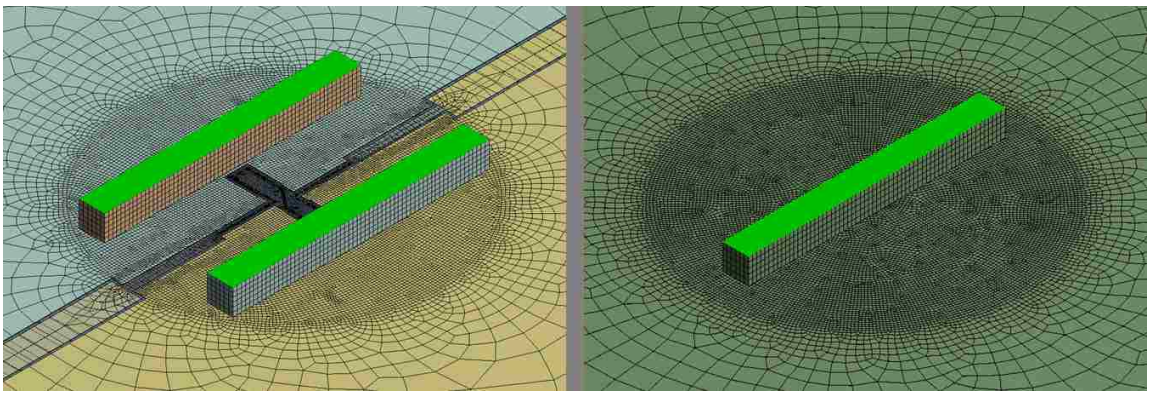

Figure 2.7: Finite element mesh of the topside copper ribbon heat sink

Figure 2.7 depicts the copper ribbon bodies integrated into the topside heat spreader models. Here, a small portion of the copper ribbon is physically modeled, while the majority is modeled as an interface resistance as defined by the

Neumann boundary condition over the highlighted lime green regions in Figure 2.7. The boundary condition coefficient accounts for $8mm$ of copper separating the block from a $23^oC$ ambient temperature (*i.e.*, the heatsink package). The outer sides of the copper blocks are assumed adiabatic while the bottoms make contact with the heat spreader through assigned Kapitza resistances. Here, a portion of the ribbon is modeled to account for some heat speeding along the width of the copper ribbon.

### CNT Array

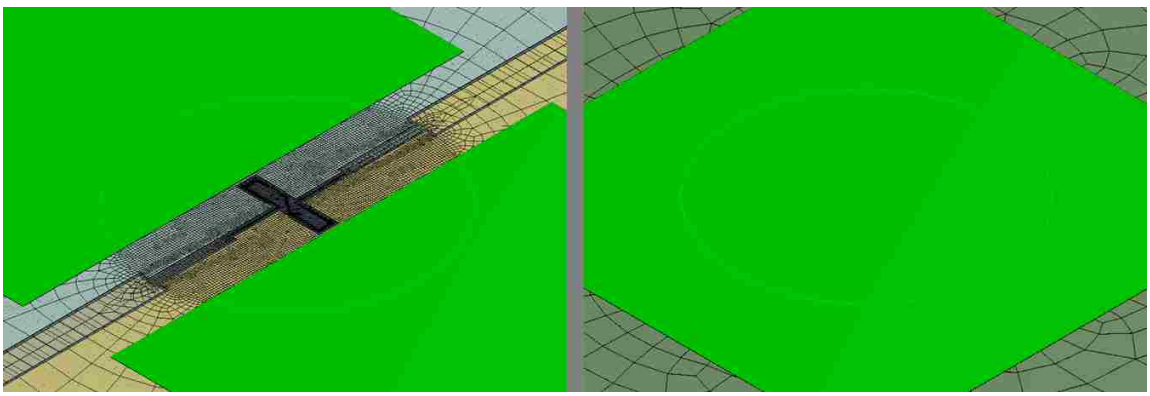

Figure 2.8: Finite element mesh of the topside CNT array heat sink

Figure 2.8 depicts the CNT array bodies integrated into the topside heat spreader models. Spanning $1mm^2$, the CNT arrays are modeled as a $1\mu$m thick body representing the nanotubes which interface the top of each heat spreader to the Neumann boundary condition highlited in lime green. Within the boundary condition, a coefficient accounts for $1\mu$m of cobalt in contact with a $23^oC$ ambient temperature (*i.e.*, the heatsink package). The nanotube body is assigned an anisotropic thermal conductivity of 1500 $\frac{W}{mK}$ in the out of plane direction, and 5 $\frac{W}{mK}$ in the in plane directions, accounting for Van Der Waals interactions. The Kapitza resistances between the cobalt, nanotubes, and spreader is approximately included in the thermal conductivity which was measured as an effective value with contacts present in the

temperature measurement [7]. The nanotube body was meshed to mirror that of the heat spreaders, conforming to the same circular refinement region with identical sizing parameters.

# Chapter 3

# Control Model Validation

## 3.1 Overview

To have confidence in the simulation results, we must first asses assigned material properties, geometries, and boundary conditions by validating the control model. There are two aspects of the control model solution that we would like to investigate. First, we would like to know if we are simulating correct temperature magnitudes for a given power input. Second, we would like to know if those temperature magnitudes are distributed correctly. If we can confirm the validity of these model characteristics, than we can be confident in incorporating solutions to manipulate them. The following outlines the methodologies utilized for said validation.

The control model is validated via two separate measurements; a qualitative measurement using a Quantum Focus Instrument (QFI) mid-wave infrared (MWIR) temperature mapping microscope, and a quantitative measurement utilizing the measured temperature dependent electrical resistance of the platinum heater. To this end, the following outlines the performance of these measurements and how they compare to the control model simulation from Chapter 2.

## 3.2 Electrical Thermometry

To quantify the temperature values in the platinum heater, we make use of the linear relationship between the temperature of a metal and its electrical resistance. This relationship is easily measured, and is known as a devices thermal coefficient of resistance (TCR). We utilize this relationship to measure temperature during operation of the micro heater through analysis of the resistance.

### Thermal Coefficient of Resistance

A TCR measurement was carried out for the microheater device on a controlled temperature plate using a Keithley 2400 source meter. A small amount of current was sourced to the heater to probe its electrical resistance while the plate's temperature was incrementally increased. Figure 3.1 contains this information, as well as the calculated TCR. Using the TCR, an electrically derived temperature, termed here TCR Temperature or $T_\Omega$, can be obtained during operation by measuring the change in resistance of the device relative to a known temperature.

This electrically derived TCR temperature does not necessarily represent a single point within the heater, however. Rather, $T_\Omega$ is an equivalent representation of the total series resistance produced by the non-uniform temperature profile (see Figure 3.3), to the temperature-resistance relationship realized under isothermal calibration. Care must therefore be taken when comparing the temperatures obtained *via* different characterization techniques. To facilitate standardized comparisons, a methodology is employed to derive a nominal heater temperature from extracted values of IR ($T_{IR}$) and FEA ($T_{FEA}$) temperature maps. The following explains how to obtain this nominal temperature from known heater geometry, measured material properties, and extracted FEA and IR heater cuboid temperatures.

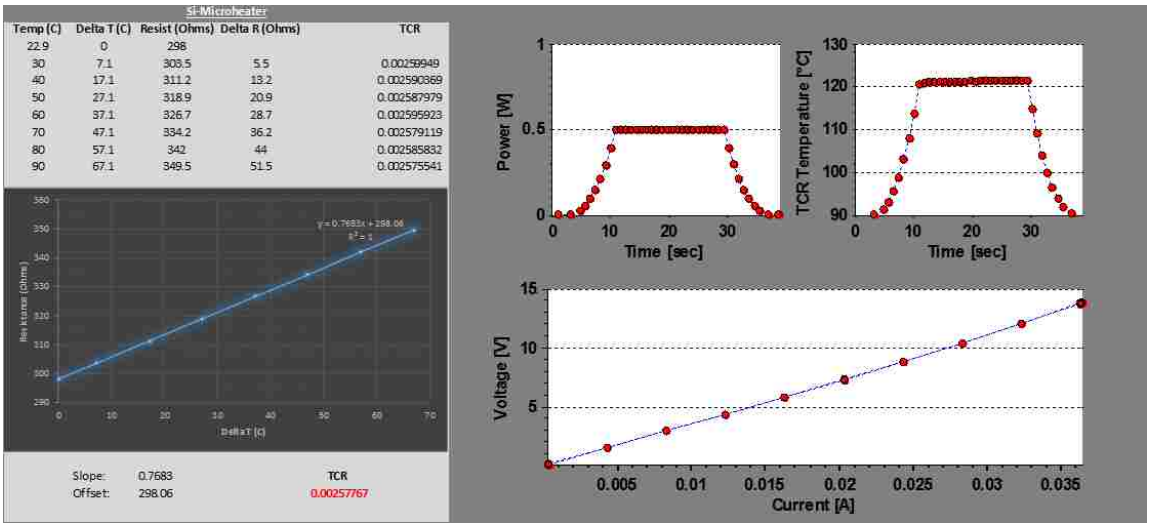


Figure 3.1: a.) Measured device TCR data, and b.) Subsequent TCR temperature of powered device shown in Figure 3.3a.

### Nominal Temperature Calculation

Nominal temperatures are calculated by utilizing Pouillet's law of resistance below.

$$R = \rho \frac{l}{A} \tag{3.1}$$

where R is resistance in ohms, $\rho$ is resistivity in ohm-m, l is length in meters, and A is cross-sectional area in $m^2$. Since the relative geometry of the heater will be largely unaffected by a change in temperature, it follows that the temperature dependence of the TCR is a function of resistivity. We use this relationship to calculate heater resistances based on known geometry and obtained temperature distributions (*i.e.*, FEA / IR thermogrpahy map). By extracting the temperature of each heater cuboid and relating it to a resistivity value, a series of cuboid resistances can be calculated that when summed together, produce a total hear resistance that can be correlated to the isothermal calibration curve. The isothermal temperature that corresponds

to the calculated total heater resistance is our nominal temperature, and can be compared to that obtained through electrical thermometry. In order to perform this calculation, device specific temperature dependent resistivity values must first be realized.

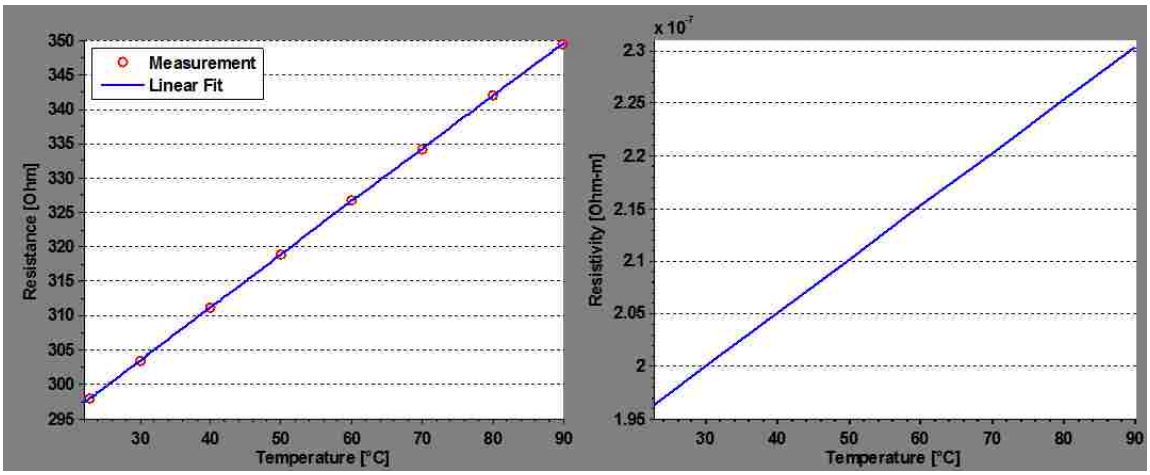


Figure 3.2: a.) Measurement of Resistance, and b.) Resistivity of the microheater for isothermal calibration

We begin by fitting the raw TCR resistance data to a line as shown in Figure 3.2a. Since the heater is at uniform temperature, we can convert resistance into resistivity from known cuboid geometry (See inset of Figure 2.1) and our temperature based linear fit via Eq 3.4 below.

$$R(T) = \sum_{i=1}^{n} \rho(T) \frac{l_i}{w_i t_i} \tag{3.2}$$

$$R(T) = \rho(T) \sum_{i=1}^{n} \frac{l_i}{w_i t_i} \tag{3.3}$$

$$\rho(T) = \frac{R(T)}{\sum_{i=1}^{n} \frac{l_i}{w_i t_i}} \tag{3.4}$$

where R(T) is temperature dependent resistance in ohms, $\rho(T)$ is temperature dependent resistivity in ohm-m, l is cuboid length in meters, w is cuboid width in meters, and t is cuboid thickness in meters.

As previously discussed, we can now use this temperature-resistivity relationship to calculate each cuboid's resistance based on individual geometries and mean temperatures extracted from FEA and IR thermography maps. Once a resistance unique to each cuboid is obtained, they can be summed together for a total heater resistance, that when extrapolated with the liner fit in Figure 3.2a, provides an equivalent temperature comparable to $T_\Omega$. This procedure is carried out for a series of model and device power inputs, with results plotted in Figure 3.4. It is shown that close correlation is obtained from the FEA and electrical based thermometry. Quantitatively, therefore, the model is validated.

## 3.3 Infrared Thermography

Infrared thermography is made possible by natural light emission, defined by Planck's distribution to be both temperature and wavelength dependent. When a body is over zero degrees Kelvin, it will emit photons over a range of wavelengths between 1-50 $\mu$m, with a concentration of increasingly shorter wavelengths as temperatures get larger. In conjunction with a shift in wavelength, the number of photons emitted will increase at an exponential rate. This provides a measurable relationship between emission and temperature, which we will use to deduce temperature maps during device operation. To facilitate, we make use of a QFI Infrascope system that utilizes an indium antimonide (InSb) sensor array to detect light in the 2-4 $\mu$m wavelength

range. The system produces temperature maps by comparing captured light intensities to the measured temperature dependent emission of a black body calibration source. By first deducing pixel emissivity through comparisons to black body emission at a uniform calibration temperature, powered temperatures can be calculated from emissivity, captured emission, and the black body calibration curve.

However, as we will see, temperature averages and issues of signal to noise can create large errors in these temperature maps. First, if emission originating within the body of a device is able to escape through semitransparent bodies above, it will add to the measured signal during calibration. This means that in order to calculate a powered temperature representative of the device surface, the entire region of signal contribution must also be at that temperature. Since there will likely be a temperature gradient instead, the calculated powered emission will correlate to a black body temperature somewhere within that gradient, thus producing a temperature depth average. Second, since we are using a microscope to concentrate light onto the sensor array, we are inherently incorporating light diffraction into the measurement. This produces signal overlap withing the focal plane, effectively incorporating a lateral average into the temperature map. Lastly, if the signal to noise of a device is too low, ambient IR light within the room will heavily influence the measured photon intensities thus altering emissivity, and therefore temperature.

With these errors in mind, we performed IR thermography measurements on the microheater device for a series of power inputs. For these measurements, the bottom surface of the substrate was held at $90°C$ and power was both supplied and measured using a Keithley 2400 sourcemeter operating in a 4-wire configuration. At each power level, measurements were performed using several objectives having lateral resolutions ranging from (2.5-24 $\mu$m). Lateral resolution was measured by analyzing the irradiance profile across a stage micrometer having sharply defined metal features patterned atop glass. Quantitatively, each objective's lateral resolution was defined

as the full width at half-maximum of the fitted Lorentzian profile resulting from the derivative of this pseudo-knife edge experiment. We then used the results to calculate nominal device temperates through the procedure described in the previous section of this chapter to compare temperature magnitudes with that of the FEA and electrical thermometry. For the highest input power investigated, a temperature map is extracted for qualitative comparison to the FEA simulation. Results and details are as follows.

As described above, infrared temperature measurements require a calibration step to measure an effective emissivity before powering the device and extrapolating temperatures based on initial conditions and captured photon intensities. This calibration is most accurate at elevated temperatures, especially for poor thermal emitters such as platinum, leading to a chosen base plate controlled temperature of 90°C. Since the materials in the device are semi-transparent to IR light, the InSb detector in the MWIR camera is actually capturing photons emitted from throughout the device, resulting in a depth average. Since this calculated temperature will most closely resemble that of the regions of the device that contribute the most signal, we do not see the temperature profile around the heater seen in the FEA simulation, as the majority of the through thickness remains at base plate temperature (see Figure 5.9 for through thickness temperature profile). In addition to depth averaging, diffraction limitations of the microscope being utilized limits the size of a feature that can be resolved, resulting in a blending of information over a finite region, often underestimating narrow temperature spikes (like hot spots). These averaging effects are among the reasons for utilizing IR thermography as primarily qualitative validation. Examining the results in Figure 3.3 shows a reasonable likeness between simulation and measurement, indicating sound model conditions.

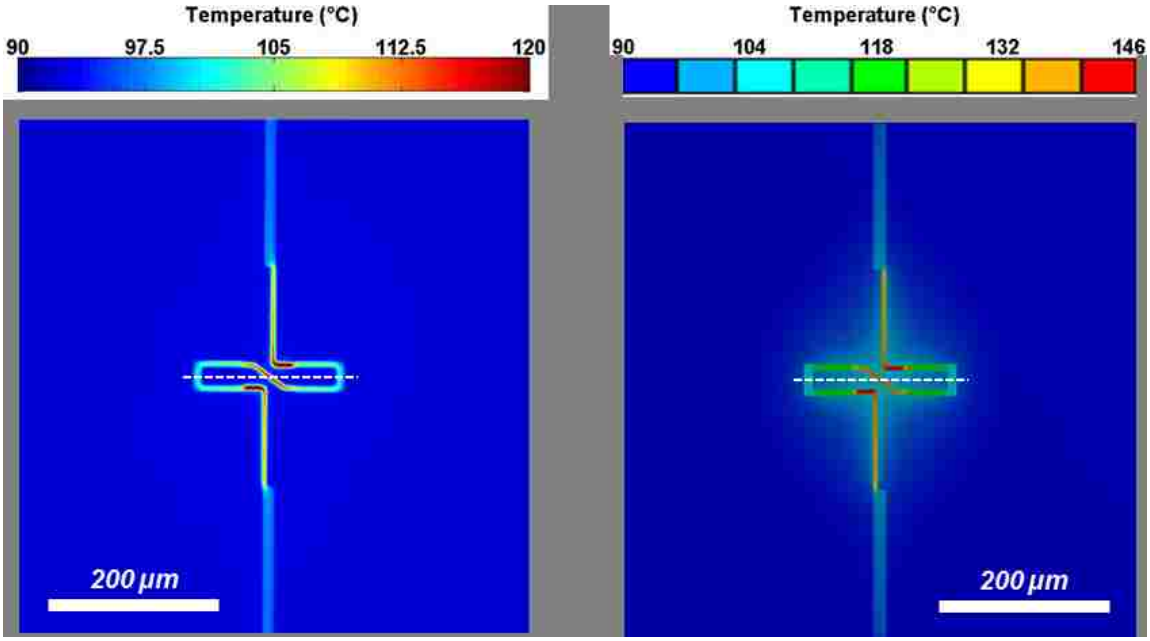


Figure 3.3: a.) IR thermography measurement map, ans b.) FEA control model simulation, both with a $90^oC$ back plate and a total power dissipation of 0.5 watts

## 3.4 Results

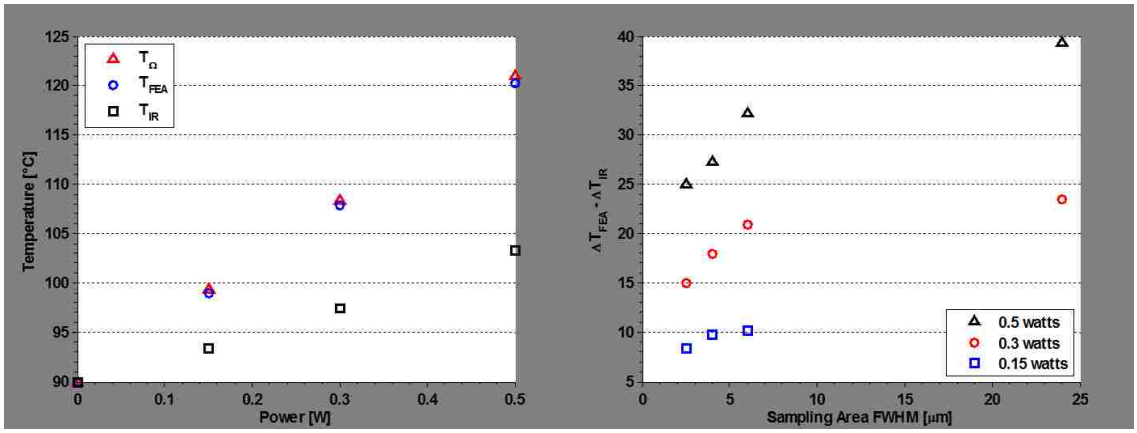


Figure 3.4: (a) Nominal heater temperatures obtained *via* each thermal characterization technique plotted as a function of power dissipation, and (b) difference in peak temperatures over the dashed lines in Figure 3.3 plotted as a function of measured IR resolution.

Shown in Figure 3.4a are the obtained nominal temperature values for each characterization method at varying power levels. It is observed that while $T_{\Omega}$ and $T_{FEA}$ are in high agreement with one another, $T_{IR}$ consistently captures significantly lower temperatures. Figure 3.4b shows how this temperature discrepancy increases as IR sampling area becomes larger with decreasing microscope numerical aperture. The depicted magnitudes and increasing trend of error represents IR averaging phenomena which will be examined in detail in a later section. Considering the high accuracy and repeatability of resistance based thermometry, coupled with the strong level of agreement between $T_{\Omega}$ and $T_{FEA}$, as well as the qualitative similarities in Figure 3.3, we can be confident in the validity of the FEA model temperatures and parameters.

# Chapter 4

# Topside Thermal Solution Results

## 4.1 Overview

Top-side thermal solutions placed upon the Pt microheater were simulated to assess their utility and compare performance. Specifically, simulations are aimed at answering three main questions. First, can the extreme thermal conductivity of graphene translate to an effective tool for thermal dissipation in realistic architectures? Second, are other carbon-based materials such as diamond or graphite of more utility? And finally, how do carbon-based solutions compare to more traditional metals frequently used in thermal solutions, such as copper?

To this end, three separate geometries are examined. First, the cooling capability of stand-alone "2-way" heat spreaders (See geometry described in Figure 1.1 and Figure 2.2) placed atop the microheater are compared. Subsequently, 3-way geometries are investigated in which the heat spreaders are connected to thermal ground via two separate conduits, composed of either copper (See geometry described in Figure 2.3 [*b*&*d*]) or carbon nanotubes (geometry of Figure 2.3 [*c*&*e*]).

## 4.2 Topside Heat Spreader Simulations

The most simplistic thermal solution is composed of a thermally conductive material, that when placed near the active region of the device, acts to "wick" heat away. Here, we examine the utility of graphene being used in this paradigm. To this end, Figure 4.1 compares the temperature reduction induced by the heat spreader for a variety of materials for both the moated and blanket spreading arrangement (See Figure 2.2). From this figure, the models indicate that the thermal solution of a heat spreader in the moated geometry is ineffective regardless of material type or thickness, resulting in less than a 5% reduction in hot spot temperature. This result is a product of heat having to travel from the heater, through the oxide, laterally, and back up through the oxide before entering the heat-spreading layers. The blanket geometry, on the other hand, provides a heat path directly into the heat-spreader layers with only 20nm of nitride separating it from the active region. The resistance offered by a 20nm SiN layer ($\frac{k}{l}$ $\frac{MW}{m^2K}$) is comparable to that of a typical thermal boundary conductance (TBC) (300 $\frac{MW}{m^2K}$). With this low resistance path, heat is able to enter the spreader and be dissipated. For this reason, comparisons between materials will center on the blanket geometry.

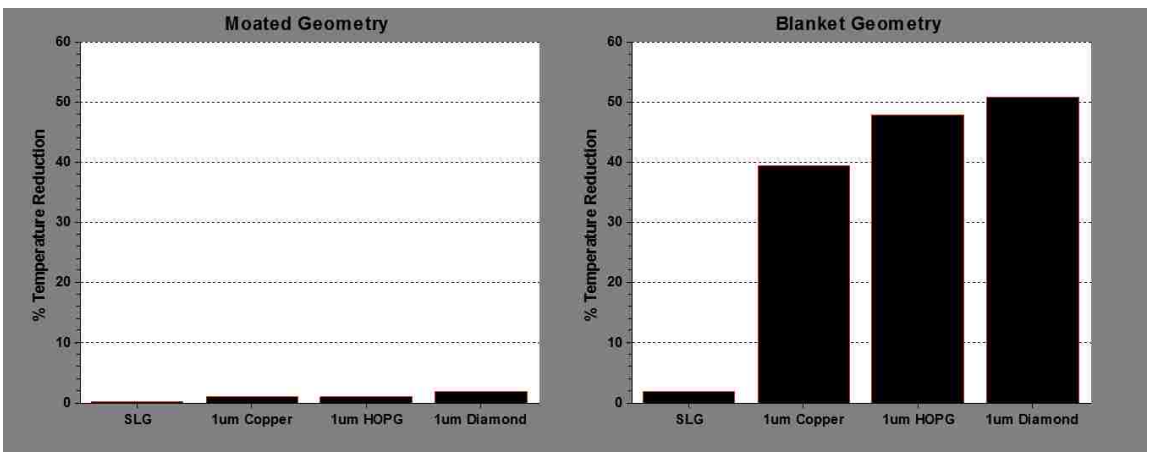


Figure 4.1: Top-side heat spreader simulation results

As shown in Figure 4.1b, the capability of a SLG heat spreader is far surpassed by materials possessing more mundane thermal conductivities. Quantitatively, a heat spreader composed of single layer graphene offers $< 2\%$ reduction of temperature as compared to the $> 40\%$ offered by $1mum$ thick layers of copper, diamond, and HOPG. This result can be attributed to the atomically thin dimension of few layer graphene, which despite its large thermal conductivity, results in an extremely small thermal conductance. Figure 4.2 shows this explicitly where the cooling capability of graphene is shown as a function of increasing layer number. The curve demonstrates that graphene becomes an effective thermal conduit as it approaches thicknesses representative of graphite, which posses both larger cross-sectional area and thermal conductivity. This increasing trend eventually asymptotes at around a $5\mu$m layer, where graphite's low out of plane thermal conductivity becomes restrictive, preventing much of the upper body from being utilized.

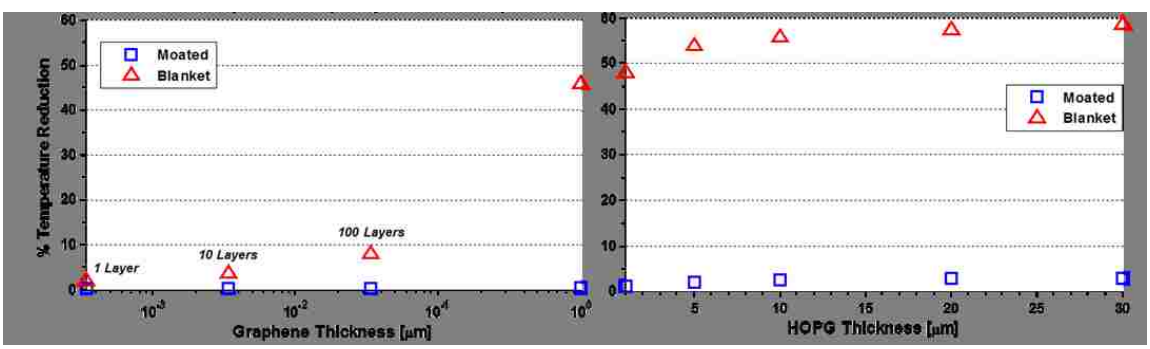


Figure 4.2: Cooling capability of a.) graphene and b.) graphite as a function of layer thickness.

Ultimately, the stand-alone heat spreader simulations allude to two main conclusions. First, in order for a heat-spreader to be effective, it must have a close proximity to heat generating regions. Specifically, the thermal path from heat generation to the spreader must be much smaller than that from generation to ground. If this is not the case, like in the moated configuration, the system will not see the spreader and the solution will remain unaffected. Second, if the heat-spreader is too thin,

it will not conduct enough heat to influence the system. Instead, a more effective solution is to implement a thick heat spreader of HOPG or diamond, or if necessary a less expensive and more practical material with moderate thermal conductivity.

## 4.3 Topside Heat Sink Simulations

In Sec.4.2, the utility of top-side thermal solutions were compared for a 2-way architecture based on heat spreading. Here, the investigation extends to the 3-way solution architecture (See Figure 1.1) consisting of a top-side heat spreader connected to the thermal sink. In this arrangement, cooling capability will be determined by not only the properties of the spreading material, but also that of the sinking CNT or copper ribbon, which include their respective interfaces. Here again, the objective of these solutions is to: (1) assess the utility of graphene in a 3-way solution (2) compare its performance versus that of other carbons and metals and (3) judge the net gain obtained by using a carbon based sinking material.

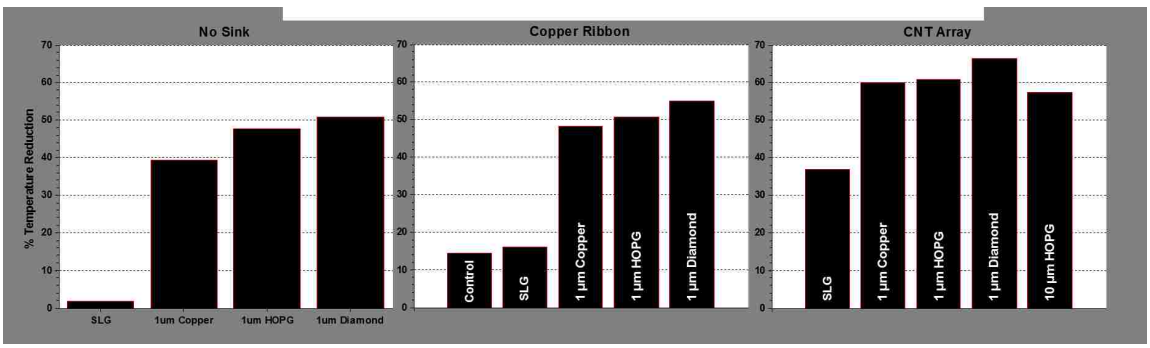


Figure 4.3: a.) 2-way stand-alone heat-spreader simulation results, b.) 3-way copper ribbon heat-sink simulation results, and c.) 3-way CNT array heat-sink simulation results

As predicted in Figure 1.1, sinking the thermal solution increases the utility of the the top-side architecture. The results are shown in Figure 4.3, where a 15%

reduction is realized by simply introducing a copper ribbon sink apart from any spreader (*i.e.*, copper ribbon control). Inclusion of a SLG spreader contributes an additional 2% temperature reduction, which is equivalent to its performance without a sink. Carrying this trend over to the CNT array suggests an approximate 35% temperature reduction from the topside sink alone, greatly outperforming the copper ribbon. This result is not surprising as the copper posses 5x lower thermal conductivity than the carbon nanotubes and achieves $< 3\%$ of contact area. We find however, that these disadvantages become less influential when better spreaders are considered. The following examines this material dependence.

Thick heat spreaders continue to offer substantial performance in the "3-way" simulations, and are the heavy lifters of the total thermal solution. While adding a heat sink will never degrade the solution, its contribution decreases as the heat-spreader becomes thicker and more conductive. For example, by adding a Cu ribbon or CNT array heat sink to a SLG heat-spreader, we see an increase in the total percent temperature reduction (PTR) of 14% and 35% respectively (see Figure 4.3). The difference between these two reductions reflects the benefits of one sink type over the other, and is termed $\Delta_{sink}$. Thus for SLG, $\Delta_{sink} = 21\%$. Similarly, adding the heat sinks to a $1\mu$m copper heat-spreader increases PTR by 8% and 20%, producing a $\Delta_{sink} = 12\%$. Performing the same analysis for a $1\mu$m HOPG spreader results in 3% and 13% for a $\Delta_{sink} = 10\%$, and 4% and 15% for $1\mu$m diamond producing a $\Delta_{sink} = 11\%$. The question becomes whether these topside sinks are worth the effort relative to their pay offs as PTR increases become relatively small, and heat-sink type contributions become more indistinguishable.

A final point to be made about the simulations regards the anisotropic nature of HOPG. We observed the impact of the anisotopy in the "2-way" heat spreader simulations as a severe asymptotic solution (see Figure 4.2). In the "3-way" configuration, we find that the restricting effects are amplified as depicted in Figure 4.3, which

shows that despite HOPG outperforming Cu in a 2-way arrangement, 10 microns of HOPG is actually worse than Cu in the "3-way" arrangement. This reduction is a result of the low out of plane thermal conductivity of HOPG, which will insulate a topside heat-sink from the system when the thickness becomes too large.

Ultimately, the top-side thermal solution simulations provide the following conclusions: (1) Graphene offers very little utility as a thermal solution when anisotropic properties, phonon scattering degradations, and atomically thin dimensions are considered. (2) For a thermal solution to be effective, its thermal path to heat generation must be less resistive than the thermal path of heat generation to ground. (3) While a heat-spreader with a large thermal conductivity will outperform that with a small, the ratio of performance to property is less than one, and anisotropy can be influential. (4) Adding a top-side heat-sink to connect a heat-spreader to ground will improve the performance of the thermal solution, albeit at a level that may not justify its inclusion.

# Chapter 5

# Simulating Infrared Thermogrphay

### Infrared Thermography

Chapter 3 outlines the basis of IR thermography as well as various sources of error associated with it. Here we will attempt to mimic the physics behind the temperature mapping technique in order to better understand these errors, and potentially remove them in a bottom up approach. We will achieve this by writing a MATLAB script that calculates the total theoretical infrared photon flux that an IR camera would detect for a given material stack and temperature profile. From this quantity, it will be possible to carry out measurement procedures on the computation, thus simulating the parameters and mechanisms responsible for the errors. The simulations will begin by computing emission based temperature over a one dimensional depth vector. This computation will produce a single temperature value which incorporates a finite depth average. Calculating this temperature depth average over the entire surface of a device produces a 2-D temperature map that must then be averaged radially with a weighting function based on the measured diffraction resolution of the IR system. The combination of these two averages produces a 2-D temperature map that represents that which an IR thermography measurement would produce, thereby

highlighting the assumptions implicit to the technique.

The steps described above are presented and discussed in the following subsections, with accompanying calculations on the control model carried out for clarification and validation. For simplicity, the procedure will be performed over a horizontal line across the center of the heater to compare line temperatures as opposed to 2-D maps. This 2-D analysis will give a good approximation of the final solution and provide at minimum a proof of concept.

## 5.1 Simulating Stack Thermal Emission

### Thermal Emission

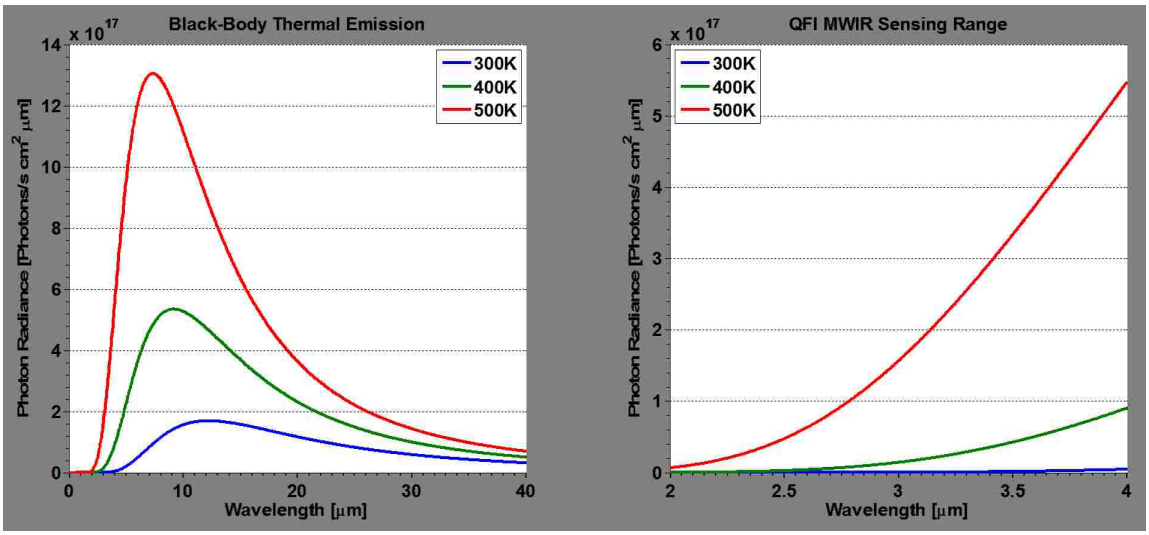


Figure 5.1: a.) Temperature Dependent Black-Body Thermal Emission, b.) over QFI MWIR sensing range.

IR thermography measurements are made possible by the phenomenon of thermal emission. When a material's thermal state corresponds to a temperature above zero degrees Kelvin, it emits photons over a wavelength range defined by Planck's

equation of thermal emission, shown in Eq 5.1 below. This equation defines a theoretical energy flux that a perfect emitter (*i.e.*blackbody) would produce, varying with temperature and wavelength .

$$Q_{BB}(T,\lambda) = \frac{2\pi hc^2}{\lambda^5}\frac{1}{exp\frac{hc}{\lambda T k_b} - 1} \tag{5.1}$$

where
$T$ = temperature, [K]
$\lambda$ = wavelength, [m]
$c$ = speed of light, $3x10^8$ [m/s]
$h$ = Planck's constant, $6.63x10^{-34}$ [Js]
$k_b$ = Boltzmann constant, $1.38x10^{-23}$ [J/K]

Owing to the fact that a photon carries energy at a rate defined by Eq 5.2 below, Eq 5.1 can be rewritten as Eq 5.3 to define the thermally emitted photon flux profile graphed in Figure 5.1.

$$E_{photon} = \frac{hc}{\lambda} \tag{5.2}$$

$$Q_{BB}(T,\lambda) = \frac{2\pi c}{\lambda^4}\frac{1}{exp\frac{hc}{\lambda T k_b} - 1} \tag{5.3}$$

This equation of blackbody thermal emission will be used as the basis for calculating stack emission. Assigning this value to every point throughout a material stack as a function of local temperature will act as an input to the simulation. The system will then determine how much of that emission will escape the stack and be observed

for measurement, which when related to that of isothermal blackbody emission, will provide the parameters necessary for deducing IR simulated temperatures.

### Emissivity

A blackbody is defined to be a perfect emitter and absorber, producing the largest number of photons per second possible for a given temperature and wavelength. For a material body to achieve this blackbody radiance, it needs to possess optical properties that result in complete opacity and no surface reflections. As the surface becomes more reflective and opacity decreases, fewer photons will originate in the body and be able to escape out the top, thus reducing the number observed. These are the factors that determine a body's emissivity, which is defined as the number of photons exiting the surface of a body relative to that produced via Eq 5.3. In order to simulate an IR thermography measurement, we must be able to calculate emissivity by predicting the total photon flux exiting a stack based on material properties and internal temperature. This will allow us to determine the stack's effective emissivity when the temperature profile is uniform and known; Having an effective emissivity, in turn, provides a correlation between increased photon intensities and temperature when the profile is unknown. We will begin building this model by considering a simple opaque body in air.

### Simulating Body Emission

The opacity of a material is related to how quickly light is absorbed as it travels through it. Mathematically this is defined by the Beer-Lambert law shown in Eq 5.4 below.

$$\frac{\phi_z}{\phi_o} = e^{-\alpha z} \tag{5.4}$$

where
$z$ = Distance from the origin of light
$\phi_z$ = Light intensity at distance z
$\phi_o$ = Light intensity at origin
$\alpha = \frac{4\pi k}{\lambda}$

The absorption coefficient, $\alpha$, is related to the extinction coefficient, $k$, which is also the imaginary part of the complex refractive index, $n$. The inverse of the absorption coefficient, termed the penetration depth, is the distance at which the intensity of light moving through a material has dropped to 1/e of its original value. Bodies with a thickness greater than about three times their penetration depth are considered opaque, as no light incident on the body will be able to escape out the other side. Therefore, when simulating light emission from an opaque body, we only need to track what happens within the semi-transparent region below the surface, and can ignore backward moving light due to its semi-infinite nature.

To simulate body emission, we need to know what percent of $Q_{BB}$, originating over the entire depth of the body, will actually exit to be observed. To calculate this depth dependent transmission, we begin by using Eq 5.4 to define the intensity of light reaching the top interface relative to the original intensity at depth $z$. The percent of light intensity that will then transmit over that interface and into the next body (*i.e.*,air) will be equal to $1 - R_{int.}$, where $R_{int.}$ is given by the Fresnel equation of Reflectance (Eq 5.5) below.

$$R_{int.} = \left(\frac{n_1 - n_2}{n_1 + n_2}\right)^2 \tag{5.5}$$

where

$n_1$ = Complex refractive index of the incident medium

$n_2$ = Complex refractive index of the transmitted medium

We thus calculate the total depth dependent photon transmission, $\phi$, by combining equations Eq 5.3, 5.4, and 5.5, into Eq 5.6 below.

$$\phi = e^{-\alpha z} Q_{BB}(T, \lambda)(1 - R_{int.}) \tag{5.6}$$

To obtain the total number of photons that the entire body will produce, we integrate $\frac{\partial \phi}{\partial z}$ over $z$, from zero to $\infty$. Also, since $Q_{BB}$ is effectively $\frac{\partial \phi}{\partial \lambda}$, we must apply a second integral over $\lambda$, with bounds defined by the IR camera's sensing capabilities. For our purposes, this will be from $2-4\mu$m. Computing the double integral depicted in Eq 5.7 produces a total number of $\frac{photons}{m^2 s}$, exiting an opaque body, with known refractive index, and at a uniform temperature T.

$$\phi_{tot.} = \int_0^{\infty} \int_{\lambda_1}^{\lambda_2} \alpha e^{-\alpha z} Q_{BB}(T, \lambda)(1 - R_{int.}) d\lambda dz \tag{5.7}$$

To verify Eq 5.7, we will numerically evaluate an emissivity and compare the result to Kirchhoff's law, which defines the emissivity of a perfectly opaque body in thermal equilibrium as 1-R. Since emissivity, $\epsilon$, equals total body emission relative to a blackbody, $\epsilon = \frac{\phi_{tot.}}{\phi_{BB}}$, where $\phi_{BB}$ is defined as Eq 5.8 below.

$$\phi_{BB} = \int_{\lambda_1}^{\lambda_2} Q_{BB}(T, \lambda) d\lambda \tag{5.8}$$

Evaluating Eq 5.7 and 5.8 for a complex refractive index of $n_1 = 3.01 + 0.051i$ (*i.e.*, n-doped silicon (nSi) at $2\mu$m), $n_2 = 1 + 0i$ (*i.e.*, air), a temperature of $500K$, and over a wavelength range of $2 - 4\mu$m, produces a photon flux of 2.98e21 and 3.98e21 $\frac{photons}{m^2 s}$ respectively. Taking the ratio of these values produces a simulated $\epsilon = 0.749$. From Eq 5.5 we calculate an $R_{int.} = 0.251$, which according to Kirchoff's law means a theoretical $\epsilon = 1 - 0.251 = 0.749$. The agreement between the two methods instills confidence in the simulation approach.

In a non-ideal system however, bodies may not be opaque, and are likely stacked together to introduce several interfaces with varying degrees of absorbing media. While our goal of calculating depth dependent transmission remains the same, many of the simplifying assumption for an opaque body will no longer be valid. For example, backward moving light will now be important to track as multiple body reflections will ultimately contribute to transmission. Additionally, our bounds of integration will now be finite and unique to each body thickness. To facilitate these requirements, we make use of the Transfer Matrix Method (TMM) to perform thin film stack optical analysis within the simulations. This method will input a defined material stack, and output wavelength dependent transmission and reflection. By applying this method to Eq 5.7, we effectively replace $e^{-\alpha z}$ and $1 - R_{int.}$ with a single $TMM_t(\lambda, z)$ term to calculate transmission. We will also need an additional refection term if the body is not opaque to include multiple reflections in the incident medium. Details of application are discussed in a later section of the chapter.

### Transfer Matrix Method

When photons are generated within the body of a device, only a fraction of that emission will be seen by the detector based on which layer it came from, and the depth within that layer that it originated. To calculate this fraction, we make use of the Transfer Matrix Method. Applying this thin film analysis technique throughout the material stack produces percent light transmission values along the depth vector based on the optical properties of the materials around it, taking into account multiple interface reflections and superposition of interfering waves. The following is a brief description of the technique as it relates to our application.

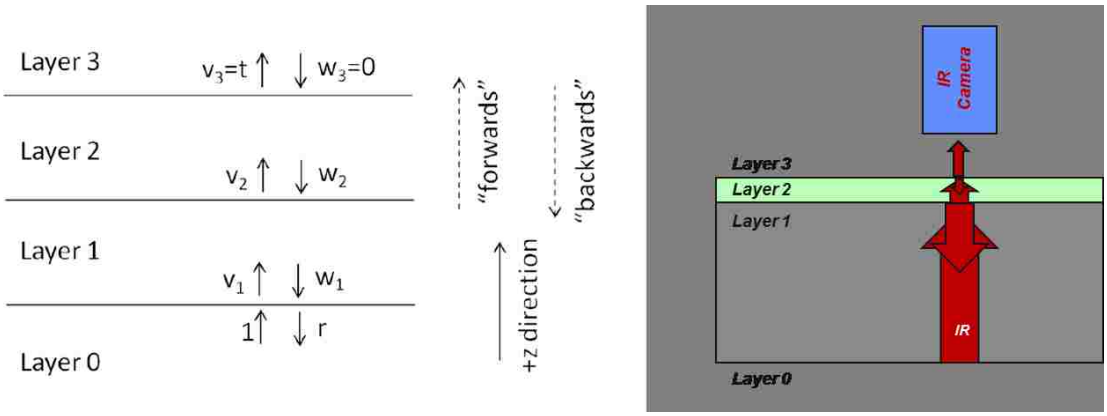


Figure 5.2: a.) Diagram of light transfer in thin film stack, and b.) Depiction of the implication in IR thermography.

The Transfer Matrix Method is driven by tracking electromagnetic wave propagation through a medium where forward-moving and backward-moving waves are superimposed, as defined by Eq 5.9 below.

$$E(z) = E_f e^{ik_f z} + E_b e^{ik_b z} \tag{5.9}$$

Assuming light propagation is normal to the layers, the forward-moving wavevec-

tor is defined as

$$k_f = \frac{2\pi n}{\lambda} \tag{5.10}$$

and the backward-moving wavevector is defined as

$$k_b = -\frac{2\pi n}{\lambda} \tag{5.11}$$

where
E(z) = the complex electric field at any given point z within a certain layer
$E_f$ = electric field magnitude of forward-moving vector
$E_b$ = electric field magnitude of backward-moving vector
n = the complex refractive index
$\lambda$ = wavelength

If the imaginary part of the complex refractive index is greater than zero, then $E_f \& E_b$ will decrease with a change in z, which simulates light absorption in non transparent bodies.

Once the forward moving wave completely traverses the medium that it was generated in, it interacts with the interface that connects it to the next layer. When this happens, a fraction of the incident wave amplitude continues moving into the next layer, and the remaining percent gets reflected back. This ratio of reflection/transmission is defined by the Fresnel equations below.

$$r = \frac{n_1 - n_2}{n_1 + n_2} \tag{5.12}$$

$$t = \frac{2n_1}{n_1 + n_2} \tag{5.13}$$

where

r = reflection coefficient (ratio of reflected amplitude to incident amplitude)

t = transmission coefficient (ratio of transmitted amplitude to incident amplitude)

$n_1$ = the complex refractive index of the incident medium

$n_2$ = the complex refractive index of the transmitted medium

For a single interface within a stack, the waves entering and leaving a specific layer through that interface can be described as

$$\begin{pmatrix} v_j \\ w_j \end{pmatrix} = M_j \begin{pmatrix} v_{j+1} \\ w_{j+1} \end{pmatrix} \tag{5.14}$$

where

$v_j$ = forward incident wave on the $j_{th}$ interface

$v_{j+1}$ = forward wave leaving the $j_{th}$ interface

$w_j$ = backward incident wave on the $j_{th}$ interface

$w_{j+1}$ = backward wave leaving the $j_{th}$ interface

where $M_j$ is the transfer matrix of the interface, and is defined as

$$M_j = \begin{bmatrix} e^{ik_{b_j} l_j} & 0 \\ 0 & e^{ik_{f_j} l_j} \end{bmatrix} \begin{bmatrix} 1 & r_j \\ r_j & 1 \end{bmatrix} \frac{1}{t_j} \tag{5.15}$$

To account for the whole material stack, a generated wave must be tracked as it transmits and reflects multiple times at each interface throughout each layer, ul-

timately producing a single forward and backward moving wave amplitude exiting the top and bottom layers respectively. We can account for all of these interactions by calculating a transfer matrix for each interface in the stack, and combining them through matrix multiplication. Doing so produces a new transfer matrix with the same dimension, but accounts for the whole stack as though it were compressed into a single layer. This effective transfer matrix is defined as

$$\tilde{M} = M_1 M_2 ... M_{N-1} \tag{5.16}$$

With the new effective transfer matrix $\tilde{M}$, we can rewrite Eq 5.14 as Eq 5.17 to output total reflection and transmission.

$$\begin{pmatrix} 1 \\ r \end{pmatrix} = \tilde{M} \begin{pmatrix} t \\ 0 \end{pmatrix} \tag{5.17}$$

where
$v_j$ became 1 (generated light entering the stack)
$v_{j+1}$ became t (transmitted light leaving the stack)
$w_j$ became r (reflected light leaving the stack)
$w_{j+1}$ became 0 (no light entering the top of the stack)

We can now solve for t and r by using the components of $\tilde{M}$ and solving as follows

$$\begin{pmatrix} 1 \\ r \end{pmatrix} = \begin{bmatrix} \tilde{M}_{11} & \tilde{M}_{12} \\ \tilde{M}_{21} & \tilde{M}_{22} \end{bmatrix} \begin{pmatrix} t \\ 0 \end{pmatrix} \tag{5.18}$$

$$t = \frac{1}{\tilde{M}_{11}} \tag{5.19}$$

$$r = \frac{\tilde{M}_{21}}{\tilde{M}_{11}} \tag{5.20}$$

Finally, we convert r and t into total power transmitted to the IR camera

$$TMM_t = |t|^2 \frac{Re\left[n_N\right]}{Re\left[n_1\right]} \tag{5.21}$$

and total power reflected

$$TMM_r = |r|^2 \tag{5.22}$$

**Simulating Stack Emission**

We can now build an expression for depth dependent photon transmission for a semi-transparent body or stack. The approach taken here is to treat every depth position, z, as a point of thermal emission between two unique material stacks. The stack above this point will include a layer of the material that the point lies in, layer j, of a thickness $z - \sum_{i=0}^{j-1} t_i$, followed by the subsequent layers $j-1:0$ above. Similarly, the material stack below this point will include a layer j of a thickness $\sum_{i=0}^{j} t_i - z$, followed by the subsequent layers $j+1:N$ below, where N is the last layer in the stack (*i.e.*, Back Plate). Figure 5.3 below depicts the approach.

As the figure shows, this method is made possible by use of the Transfer Matrix Method, which converts the entire system into a point of thermal emission sandwiched between two effective interfaces. From this simplified model, we can calculate total transmission through $T_f$, $R_f$, and $R_b$. The total depth dependent emission will begin with $T_f$, which is the forward moving light that will escape the stack on the

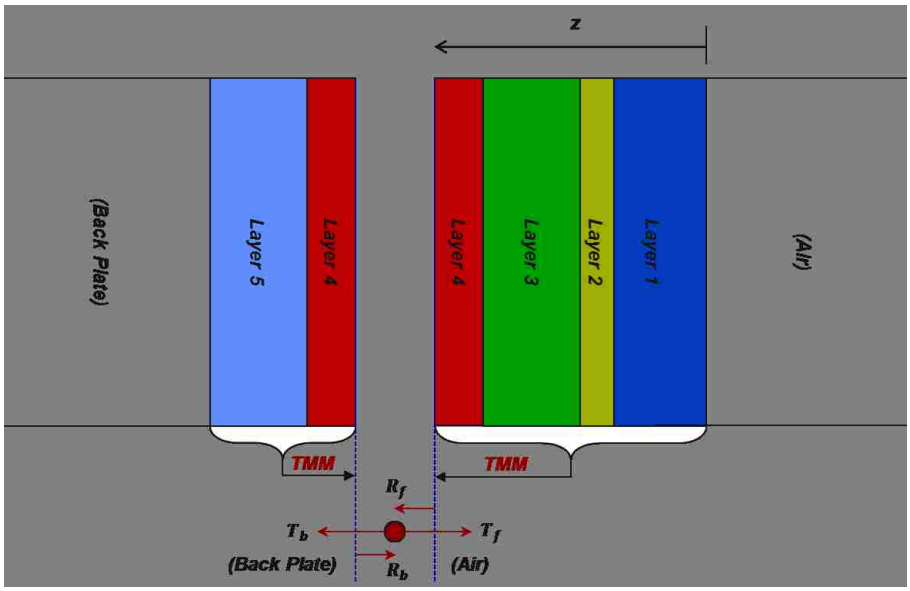


Figure 5.3: Diagram of the depth dependent stack transmission parameters and approach.

first pass within layer j. However, some percent of that forward moving light will reflect back to the point of origin, which is represented by $R_f$. That reflection will then travel backward through the lower stack, where a certain percent will be reflected back up to the point of origin, represented by $R_b$. This twice reflected forward moving light will then have another opportunity to transmit out of the stack based on $T_f$, where the cycle will repeat. Repeating this cycle an infinite number of times will produce the total percent transmission of the forward moving light, $\gamma_f$, which can be mathematically represented by Eq 5.23 below.

$$\gamma_f = T_f + R_f R_b T_f + R_f^2 R_b^2 T_f + R_f^3 R_b^3 T_f + ... + R_f^\infty R_b^\infty T_f \tag{5.23}$$

Substituting $P = R_f R_b$, and factoring out $T_f$ gives the following expression.

$$\gamma_f = T_f(1 + P + P^2 + P^3 + ... + P^\infty) \tag{5.24}$$

We recognize the infinite summation in parentheses as the Maclaurin series for $(1-P)^{-1}$, resulting in a total percent transmission of $\gamma_f = T_f(1-R_fR_b)^{-1}$. Carrying out the same procedure for light that is originally emitted backwards, will produce a similar expression of $\gamma_b = T_fR_b(1 - R_fR_b)^{-1}$, as there will be one extra backward reflection in each summation term. The total percent transmission of the point thermal emission is therefore $\gamma_f + \gamma_b$, which is given in its final form in Eq 5.25 below.

$$\gamma = T_f(1 + R_b)(1 - R_fR_b)^{-1} \tag{5.25}$$

The full expression for depth dependent photon transmission is thus obtained by combining Eq 5.3, and 5.25, where the terms in Eq 5.25 are ideally obtained from the Transfer Matrix Method. It is known however, that TMM is only valid when the incident medium is non absorbing. When this is not the case, extra absorption at the first interface induced by constructive light interference does not get factored into the energy equations, resulting in inaccurate outputs. We overcome this issue for $T_f$ by flipping the stack in the transfer matrix, so that light is incident from air, and transmits to the emission point at depth $z$. This assumption, that transmission through a stack is independent of which side it enters, can be tested with TMM for an example multilayer material stack in which both sides are non absorbing. Through this exercise, we find that while transmission is independent of direction, reflection and absorption will vary. We therefore need a method for calculating $R_f$ and $R_b$ to apply to Eq 5.25. As a first order approximation, we develop expressions based on Eq 5.4 and 5.5. We will use these equations to calculate the intensity of light

that will traverse through the incident medium, hit the first interface it encounters, and travel back to the point of emission. While in reality some percent of that light will enter the next layer and return through reflections, we will neglect these higher order reflections for simplicity. Mathematically, this $R_f$ and $R_b$ can be represented by Eq 5.26 and 5.27 below.

$$R_f = \left(e^{-\alpha_j(z-\sum_{i=0}^{j-1} t_j)}\right)^2 R_{j:j-1} \tag{5.26}$$

$$R_b = \left(e^{-\alpha_j(\sum_{i=0}^{j} t_j - z)}\right)^2 R_{j:j+1} \tag{5.27}$$

Finally, the depth dependent photon transmission for a semi-transparent body in a material stack can be written as Eq 5.28 below.

$$\phi = Q_{BB}(T,\lambda)\gamma(z,\lambda) \tag{5.28}$$

where $\gamma$ makes use of TMM for $T_f$, and Eqs 5.5, 5.26, and 5.27 for $R_f$ and $R_b$. Again, to calculate total stack emission, we first calculate $\frac{\partial\phi}{\partial z}$. From Eq 5.7, we know that $\frac{\partial\phi}{\partial z} = \alpha e^{-\alpha z}$ times some constant related to emission and transmission. Since the $e^{-\alpha z}$ and transmission terms are now both in $\gamma$, we assume that $\frac{\partial\phi}{\partial z} = \alpha Q_{BB}(T,\lambda)\gamma(z,\lambda)$, as impedance from other bodies and interfaces will be a constant as z changes in a given layer. This assumption necessitates that we calculate total emission for each layer independently however, as each layer will have a unique $\alpha$. Applying this stack summation and integrating over both $z$ and $\lambda$, produces the final expression for total photon flux emitting from a material stack at a uniform temperature, and with known refractive index values.

$$\phi_{tot.} = \sum_{j=1}^{N-1} \int_{\lambda_1}^{\lambda_2} \int_{\sum_{i=0}^{j-1} t_i}^{\sum_{i=0}^{j} t_i} \alpha_j Q_{BB}(T,\lambda)\gamma_j(z,\lambda)dzd\lambda \tag{5.29}$$

To verify Eq 5.29 we simulate thickness dependent emissivity for a single body suspended in air. Computationally, we model this as a three layer material stack where the first and last layers (layers 0 and 2) possess a refractive index of air and a thickness of zero. By varying the thickness of layer 1, we influence total emission by changing its level of opacity until reaching a thickness of about three times its penetration depth, where the solution becomes asymptotic at an emissivity of $1 - R$. We then compare the simulation results to the solution published by McMahon [24], which generalizes Kirchhoff's law for partially transparent bodies, taking both reflectivity and transmissivity into account through the following equations.

$$\epsilon = \frac{(1-R)(1-T)}{1-RT} \tag{5.30}$$

where the reflectivity R is defined as

$$R = \frac{(n-1)^2 + k^2}{(n+1)^2 + k^2} \tag{5.31}$$

and the transmissivity is given by

$$T = exp(\frac{-4\pi kt}{\lambda}) \tag{5.32}$$

where

n = real part of refractive index

k = imaginary part of refractive index

$\lambda$ = wavelength

t = thickness of the body

Below is a figure plotting the simulation emissivity vs. Eq 5.30 for two example materials. These materials are chosen as extremes in the absorption spectra, with highly absorbing platinum on the left, and nearly transparent $SiO_2$ on the right.

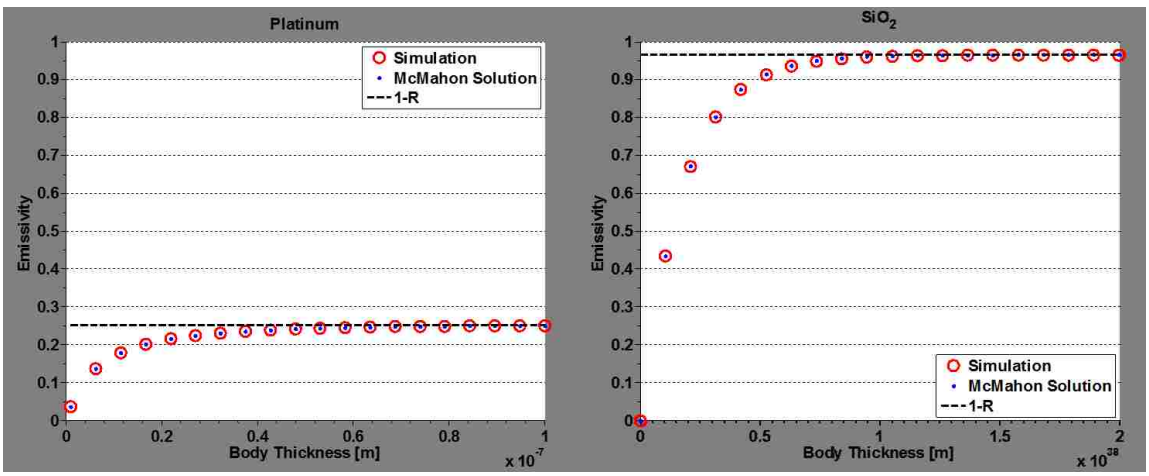


Figure 5.4: Simulated vs analytical emissivity of a.) Platinum, and b.) $SiO_2$ for varying body thickness in air.

The data in Figure 5.4 shows good agreement between our semi-transparent body simulation and both McMahon's solution and Kirchhoff's law, providing further confidence in the simulation approach. It should be noted however that the simplifying assumptions of Eqs 5.26 and 5.27 introduce zero error in this instance, since the only stack reflections are from the included interfaces. It is also interesting to note how a nearly transparent body such as $SiO_2$ can potentially approach blackbody emission, merely requiring a body thickness on the order of 4 quadrillion times the distance from Earth to the Andromeda Galaxy. For a thickness on the order of solar system length scales however, the emissivity of $SiO_2$ is essentially zero.

The analysis presented above assumes uniform body temperate and optical properties independent of wavelength. These assumptions were implemented to facilitate comparisons to the McMahon solution and Kirchhoff's law. In reality however, refractive index can vary significantly with wavelength, affecting several aspects of the simulation. We must therefore implement these dependencies to accurately simulate infrared thermography. Practically, these implementations are achieved through interpolation functions created from literature and database properties, and FEA simulation temperature profiles. Using these interpolation functions, properties and temperatures for any input within the bounds of the simulation can be called on and passed around by the numerical integration function. Implementation thus requires little alteration to the code and procedure.

Lastly, since Eq 5.29 does not include the backplate in the summation (*i.e.*,layer N), we need to add its thermal emission contribution separately. In the QFI system we wish to simulate, the temperature controlled backplate is made of aluminum, which has a penetration depth orders of magnitude smaller than its thickness. We can therefore treat the layer as opaque, and utilize a variation of Eq 5.7. The only difference is that the $1 - R_{int.}$ term will be computed by $TMM_t$, with an input of the full stack, assigning layer N a thickness of zero.

The final expression for total simulated stack thermal emission that will be used in the following sections is presented in Eq 5.33 below.

$$\begin{aligned}\phi_{tot.} = &\sum_{j=1}^{N-1} \int_{\lambda_1}^{\lambda_2} \int_{\sum_{i=0}^{j-1} t_i}^{\sum_{i=0}^{j} t_i} \alpha_j(\lambda) Q_{BB}(T(z), \lambda) \gamma_j(z, \lambda) dz d\lambda \\ &+ \int_{\lambda_1}^{\lambda_2} \int_{0}^{\infty} \alpha_N(\lambda) e^{-\alpha_N(\lambda) z} Q_{BB}(T_{cal}, \lambda) T_{f_{N:0}}(\lambda) dz d\lambda\end{aligned} \tag{5.33}$$

## 5.2 Simulating Infrared Depth Average

Utilizing Eq 5.8 and 5.33 we can carry out measurement procedures on expected temperature profiles to simulate the first source of measurement error, a depth average. Depth averages occur when signal originating within the device is able to transmit through the upper layers to contribute to the measurement. The deeper into the device signal can penetrate from, the more severe the depth average. This error begins with an isothermal calibration, which relates a measured photon intensity to a given temperature. From this point on, thermal emission to temperature comparisons will be completely based on isothermal conditions. This means that the only time a temperature is truly representative of the focal plane (*i.e.*, a device's surface), is if the entire region of signal origin is at a uniform temperature. When a thermal gradient is present however, the total measured photon emission will end up correlating to an isothermal temperature somewhere within that gradient. The exact value will depend on where the majority of signal comes from, and how steep the temperature gradient is. We obtain this value by following measurement procedures presented below.

Temperatures from an IR thermography measurement are obtained via comparisons to a blackbody calibration source. Within the system's software, values of measured camera counts (*i.e.*, photon emission) induced by a blackbody, are correlated to isothermal temperatures. When a device is placed under the camera to be measured, it is fist elevated to a controlled uniform temperature, $T_{cal}$. The camera then captures a radiance map of the device, and camera counts at each pixel are normalized to corresponding blackbody values. The product is an emissivity map that is used to determine how much signal each pixel expects to get for a given change in temperature. The device is then powered where a thermal gradient is produced between regions of heat dissipation and the constant temperature back plate. Once the device has reached steady state, a second radiance map is captured over the

same region as before. Each pixel is then divided by its corresponding emissivity value, producing a new map that represents blackbody radiance values for the elevated temperatures in the powered device. The blackbody calibration data is then referenced, and a final map with representative blackbody temperatures is created.

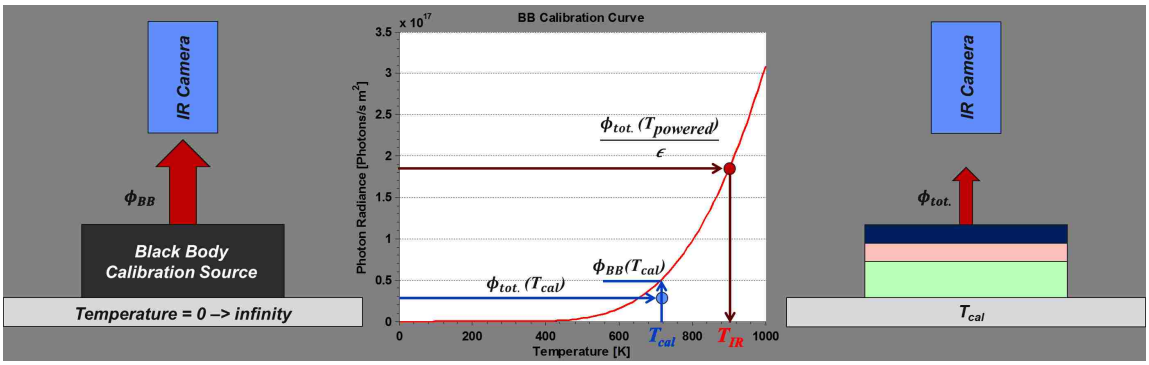


Figure 5.5: Diagram depicting an IR thermography procedure using Eq 5.8 and 5.33

The procedure described above is depicted in Figure 5.5, and is mathematically represented by the following. We first simulate the isothermal emissivity calibration by evaluating Eq. 5.33 at a uniform temperature $T_{cal}$ (ie, $\phi_{tot.}(T_{cal})$), over a $2-4\mu$m wavelength. We then evaluate Eq 5.8 at the same calibration temperature and wavelengths (*i.e.*, $\phi_{BB}(T_{cal})$), and compare the values to produce emissivity, $\epsilon$. Eq. 5.33 is then re-evaluated with a prescribed z dependent temperature profile obtained from a thermal model to produce $\phi_{tot.}(T_{powered})$. This elevated value of photon emission is then divided by emissivity (*i.e.*, $\frac{\phi_{tot.}(T_{powered})}{\epsilon}$) and is used as a target for finding a temperature $T_{IR}$ that would correspond to an equivalent $\phi_{BB}$. The temperature $T_{IR}$ is the final product of the depth average, and is ideally calculated over the entire device, and at intervals no smaller than the IR system's pixel resolution. For our purposes we will calculate this value over the line shown in Figure 3.3, and with $1\mu$m intervals.

## 5.3 Simulating Infrared Diffraction

The next step in our simulation accounts for averaging errors in IR thermography measurements arising from light diffraction. Owing to the nature of diffracted light, a microscope objective will collect photons over a finite area within the focal plane, and focus the combined signal onto a single pixel of the sensor array. This diffraction phenomenon is described by the Abbe diffraction limit, and is defined below.

$$d = \frac{\lambda}{2nsin\theta} \tag{5.34}$$

where
d = smallest resolvable spot size
$\lambda$ = wavelength
n = refractive index of the medium between the sample and objective
$\theta$ = angle associated between focal distance and lens radius

This smallest resolvable spot size is the systems diffraction limitation and is observed in the measurement as a blending of information, resulting in the distortion of sub-wavelength structures. To account for this, the depth averaged temperatures are averaged together with a spatial weighting function unique to each system, which can be measured using a precision micro-resolution target.

To extract this weighting function, we begin by taking radiance line scans over a precision resolution target. By counting the number of data points over each target spacing of a known distance, we can calculate pixel resolution. Once the pixel resolution is know, the radiance data from the line scans can be re-plotted as a function of distance (see Figure 5.6a). Notice that the data is rounded were we would expect step edges. This is the averaging we want to quantify. We then take the numerical derivative of the data with respect to distance, which results in a

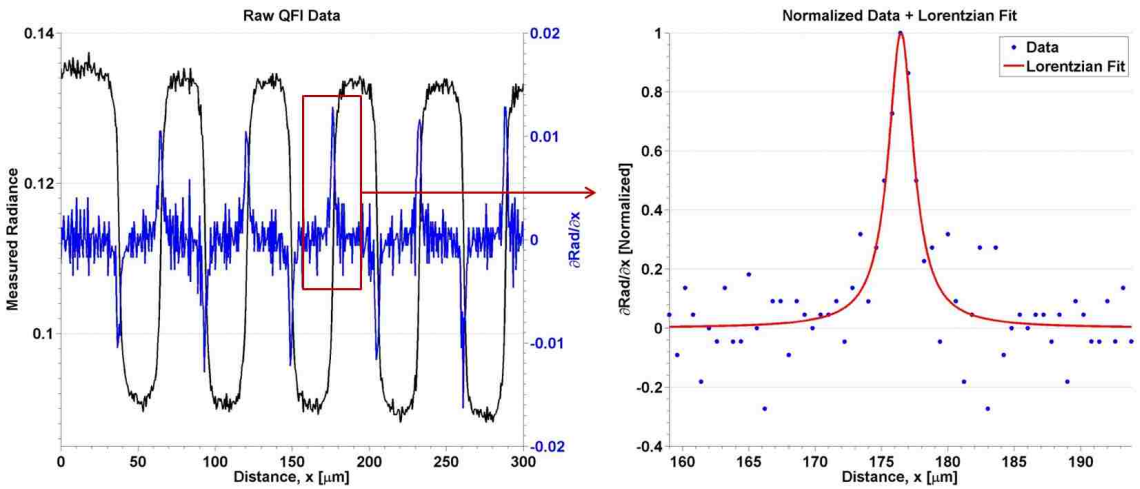


Figure 5.6: a.) Measured radiance profile over a precision resolution target and its spacial derivative, and b.) Lorentzian fit to the derivative data.

series of spikes at each oscillation point. Extracting one of these spikes, normalizing it, and fitting the data to a Lorentzian curve gives us our weighting function (see Figure 5.6b).

Below is the formula for the Lorentzian function, which we will incorporate as our spatial weighting function on temperature values surrounding a location represented by a pixel in a sensor array.

$$L(G, x, x_o) = \frac{G^2}{4[(x - x_o)^2 + (\frac{1}{2}G)^2]} \tag{5.35}$$

where

$G$ = the full width at half max of the peak

$x$ = position along the weighting function

$x_o$ = center of the peak (pixel location)

Multiplying this function along $x$ values from the temperature profile, summing the products, and then dividing by the area under the Lorentzian curve produces a single temperature value that is assigned to the location $x_o$. This value is defined as $T_{pixel}$ and is displayed below.

$$T_{pixel} = \frac{\int_{x_{min}}^{x_{max}} L(G, x, x_{pixel}) * T(x) dx}{\int_{x_{min}}^{x_{max}} L(G, x, x_{pixel}) dx} \tag{5.36}$$

By applying this function to the depth averaged temperature profile using a measured $G$ value at a periodic spacing corresponding to the measured pixel resolution, we create a new temperature profile that is representative of the final solution.

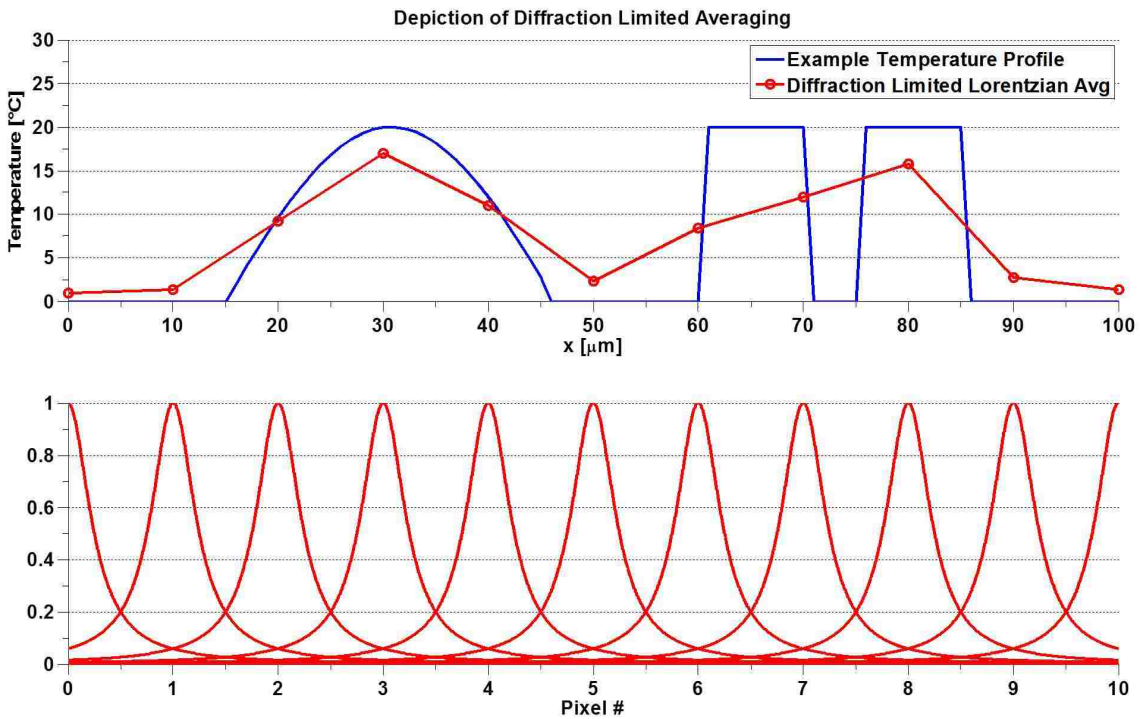


Figure 5.7: Depth averaged Si-microheater line temperature with example diffraction limited pixel temperature (top) and the corresponding spacial Lorentzian pixel weighting functions (bottom).

To illustrate the effects of diffraction averaging, we apply Eq 5.7 to an example temperature profile consisting of half a sine wave, spaced 15$\mu$m away from two step functions, separated by a 5$\mu$m distance. Below this temperature profile shown in Figure 5.7, are a series of Lorentzian weighting functions with an arbitrary value of $G$, and spacings corresponding to a pixel resolution of $10\frac{\mu\text{m}}{pix}$. By applying Eq 5.36 at each pixel location, the red temperature profile labeled "Diffraction Limited Lorentzian Avg" is produced. This temperature profile has a data resolution equal to the defined pixel resolution, and contains temperature errors proportional to the parameter $G$. We see two types of error; an underestimation of temperature, and a distorted profile. While the sine wave is represented fairly well, the two step functions are too close together for the resolution parameters of the theoretical system simulated, and are ultimately seen as a single feature. If the $G$ parameter became smaller, temperature magnitudes would improve in accuracy, though the step functions would remain to be seen as a single feature unless the pixel resolution improved.

This concludes the procedure for obtaining the full model of simulating IR thermography. In the next section we apply the theory to the control model using material properties obtained from measurement and literature, and diffraction parameters measured for various objectives.

## 5.4 IR Simulation on Control Model

We will now apply the discussed theory to the control model and carry out a series of comparisons. We start by comparing the FEA model surface temperature to IR thermography temperatures over the line profile previously discussed. This will illustrate the type and magnitude of error typically associated with IR thermography. Geometry and properties employed in the depth average simulations are then presented, and results are compared to the first two line temperatures. Measured

diffraction parameters are then presented and applied to depth average profile to produce a complete full model temperature profile.

### FEA vs IR Thermography

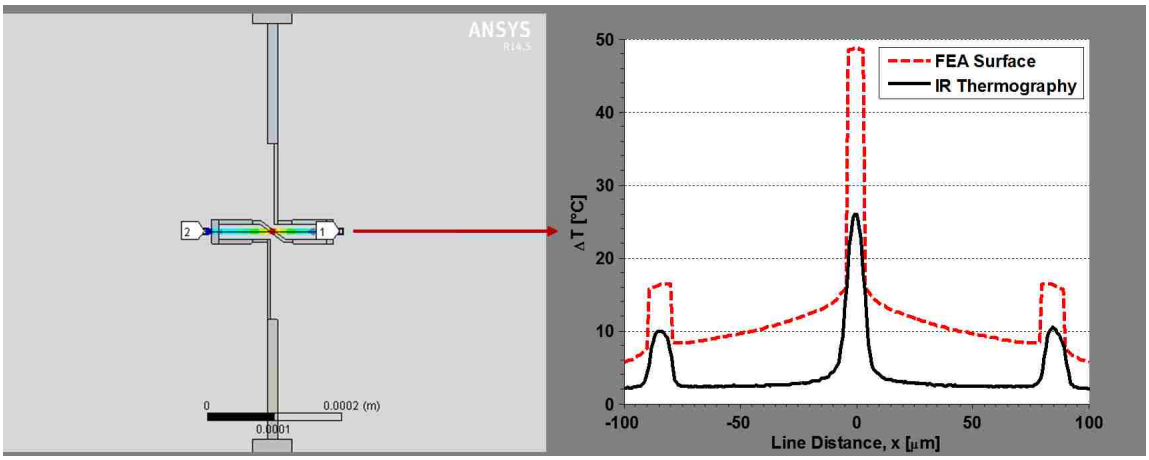


Figure 5.8: b.) FEA surface temperature vs measured IR temperature over the line depicted in (a).

Figure 5.8 contains two images, the first depicting the line temperature to be analyzed, and the second comparing FEA model to IR measurement temperatures. There are two distinct differences between them. First, their magnitudes are dissimilar, showing a percent $\Delta T$ error of nearly 50% over the heater regions, and around 80% over the silicon. The second discrepancy lies in the shape of the profile. Temperatures extracted from the model show sharp transitions from heater to $SiO_2$ and relatively flat profiles over the heater segments, while the measurement shows wider sloping transitions with rounded peaks throughout the profile.

By applying the IR simulation procedure to the FEA profile we will be able to relate these two profiles, therefore providing additional validation to the model and confidence in our measurement. We will begin by discussing the parameters enforced on the depth average model.

### Depth Averaging

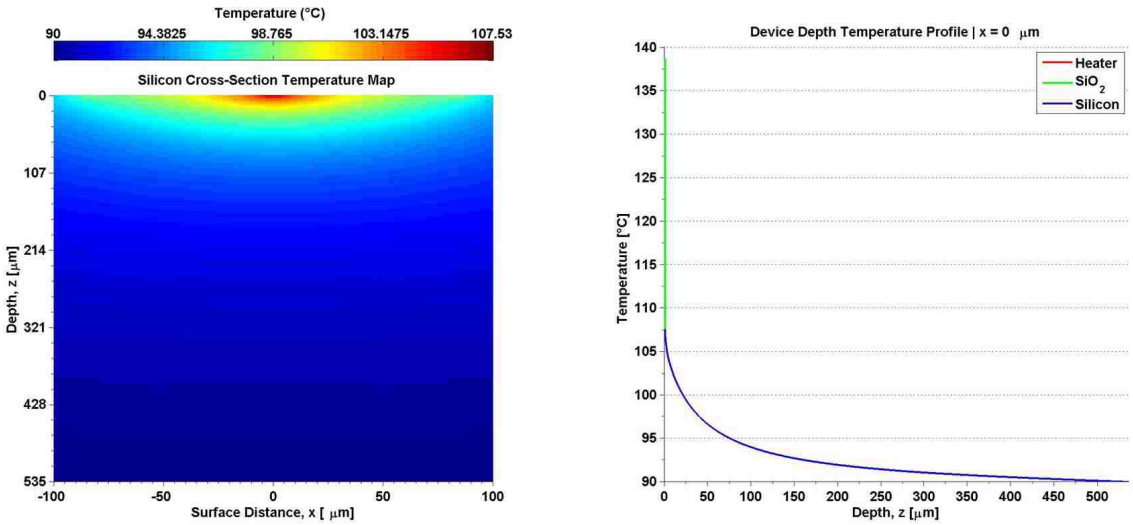


Figure 5.9: a.) Silicon substrate cross-sectional temperature map, and b.) Extracted line temperature profile with scaled heater and oxide profiles for depth average.

Table 5.1: Material Stack Optical Properties

| **Material** | **Function** | **Thickness** | **Avg k** | **Avg n** | **Source** |
|---|---|---|---|---|---|
| Pt | Heater | 100 nm | 10.2 | 3.69 | refractiveindex.info |
| Ti | Adhesion | 10 nm | 4.32 | 3.65 | refractiveindex.info |
| $SiO_2$ | Dielectric | 300 nm | 4.16e-11 | 1.43 | SNL |
| nSi | Substrate | 535 $\mu$m | 9.48e-5 | 3.53 | P. J. Timans |
| Al | Back Plate | Semi-Inf | 28.4 | 4.07 | refractiveindex.info |

Table 5.1 contains informations on the properties and dimensions of the total material stack simulated in the depth average.

Due to the semiconductor nature of the lightly doped silicon substrate, its emission properties will vary as available carriers increase with increasing temperature. The semi-empirical model provided by Timan [25] is for lightly doped silicon of similar dopant concentrations as our device, and accounts for a temperature dependence ranging from approximately $270^oC$ to over $800^oC$. Since we do not know the exact

properties of our silicon substrate, we use this empirical model to provide refractive index values that result in a simulated stack emissivity comparable to the IR thermography measurement. These refractive index values, which are well within reason for a silicon wafer, produce an emissivity of 0.38 with over 90% signal contribution originating in the silicon, as obtained through the stack thermal emission simulations.

Since we are attempting to simulate measurement parameters, we will include an IR ambient noise term in the simulations as well. This ambient IR signal is low enough to only influence measurements over low emitters such as metals, and can be extracted from an IR thermography emissivity map. It is observed that the measured emissivity of a metal is always larger than the theoretical value produced by Kirchhoff's law. We attribute this overestimation to ambient IR noise, which tuns out to be on the order of a body's thermal emission at $20^oC$. We quantify this value by calculating the blackbody radiance required to produce the difference in measured to simulated emissivity as shown in Eq 5.37 below.

$$\phi_{amb.} = (\epsilon_{meas.} - \epsilon_{sim.}) \int_{2\mu\text{m}}^{4\mu\text{m}} Q_{BB}(T_{cal}, \lambda) d\lambda \tag{5.37}$$

For a measured and simulated emissivity of 0.1 and 0.0665 respectively, we calculate a $\phi_{amb.}$ at $90^oC$ of 5.95e18 $\frac{photons}{m^2 s}$. We incorporate this value into the depth averaging simulations via Eq 5.38 and 5.39 below.

$$\epsilon = \frac{\phi_{tot.}(T_{cal}) + \phi_{amb.}}{\phi_{BB}(T_{cal})} \tag{5.38}$$

$$\phi_{BB}(T_{IR}) = \frac{\phi_{tot.}(T_{powered}) + \phi_{amb.}}{\epsilon} \tag{5.39}$$

Next we define the depth dependent temperature profile for the powered device. The layers associated with the heater are all assumed to be at a uniform temperature which is extracted from the Pt body in the model. Since the $SiO_2$ layer is modeled as a boundary conductance in the FEA simulation, we do not know its exact temperature profile. However since heat is dissipated through it and into the substrate, we know that its temperatures will be between that of the heater and of the top of the silicon. We therefore assume it to be a linear interpolation between the two. Lastly, depth line temperatures from the silicon substrate are extracted over the line of interest at increments of 1$\mu$m over a 200$\mu$m region, and placed into the columns of a matrix in MATLAB, imaged in Figure 5.9a. The depth averaging program uses this map by taking one column at a time and tacking on the appropriate heater temperature and $SiO_2$ profile, such as that shown in Figure 5.9b. The $SiO_2$ layer is assumed to be at a uniform temperature equal to silicon's surface temperate over regions of the device between and outside of the heater.

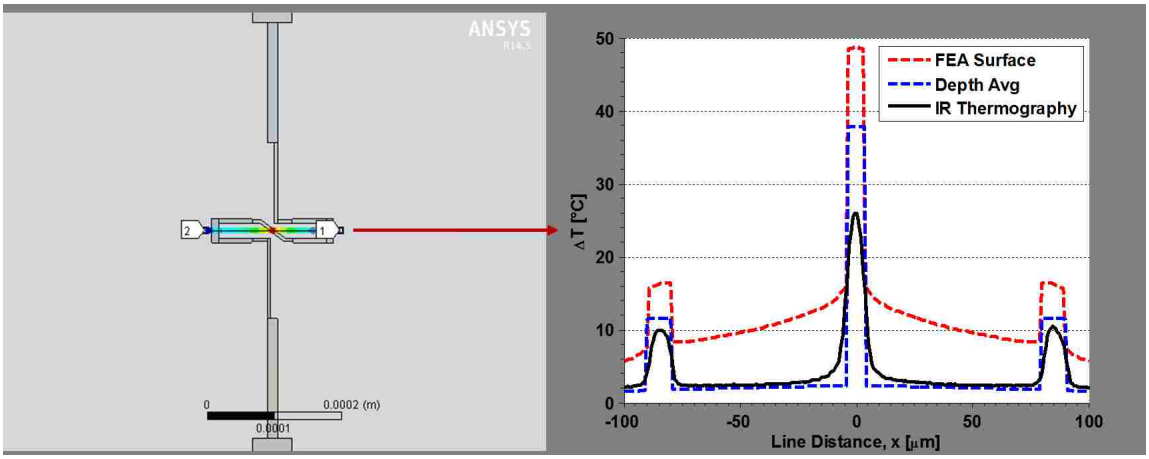


Figure 5.10: b.) FEA surface temperature with depth average vs measured IR temperature, over the line depicted in (b).

Running these temperature profiles with their respective geometries and optical properties through the depth averaging simulations produces the line temperature in Figure 5.10. We can see that the magnitude of error between the new temper-

ature profile and the measurement has been significantly reduced, especially over the non-heater regions. However since diffraction has not been considered yet peak temperatures remains too high and the profile transitions remain to sharp.

### Lateral Averaging

Next we apply the Lorentzian lateral weighting function to the depth averaged temperature profile according to several measured parameters.

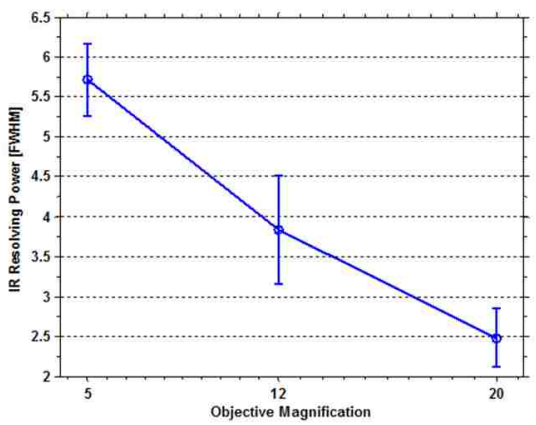


| Objective | Pixel Resolution | |
|---|---|---|
| | pixels/um | um/pixel |
| 1x | 0.0829 | 12.06 |
| 5x | 0.4105 | 2.44 |
| 12x | 0.9701 | 1.03 |
| 20x | 1.6624 | 0.60 |

Figure 5.11: Measured a.) full width half max parameter $G$, and b.) pixel resolution, for various objective magnifications on an MWIR QFI Infrascope.

Figure 5.11 contains measured resolution data for the system and magnifications used to perform IR thermography on the micro heater device. Using the mean values for the 20x objective, and applying Eq 5.36 over the depth averaged line temperatures produces the new profile depicted in Figure 5.12 below. This final profile includes the full model discussed in this chapter utilizing data and parameters either measured, simulated, or obtained from literate.

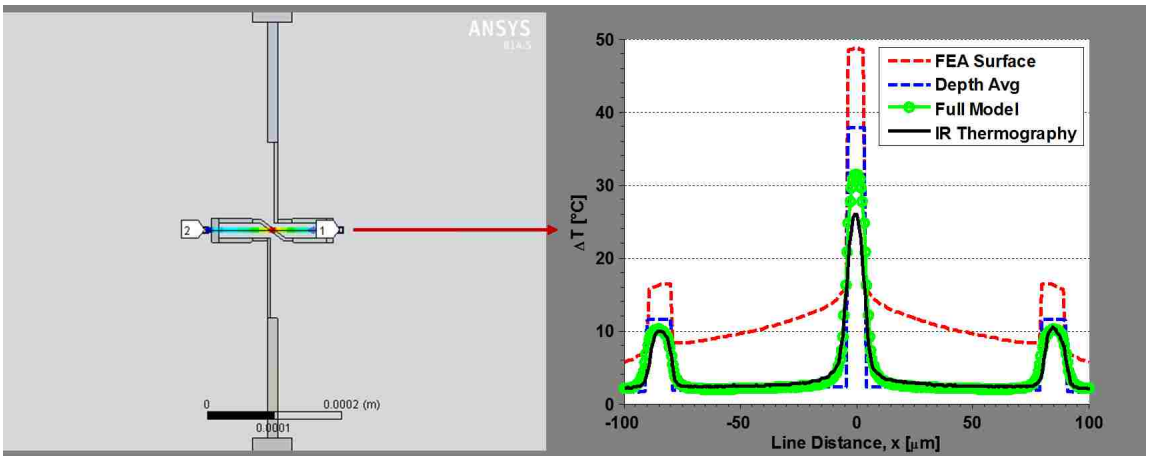


Figure 5.12: b.) FEA surface temperature with full simulation vs measured IR temperature, over the line depicted in (a).

### Full Model

Performing the full simulation procedure with temperature profiles for various FEA model power inputs at each measured diffraction and resolution parameters produces the following array of figures.

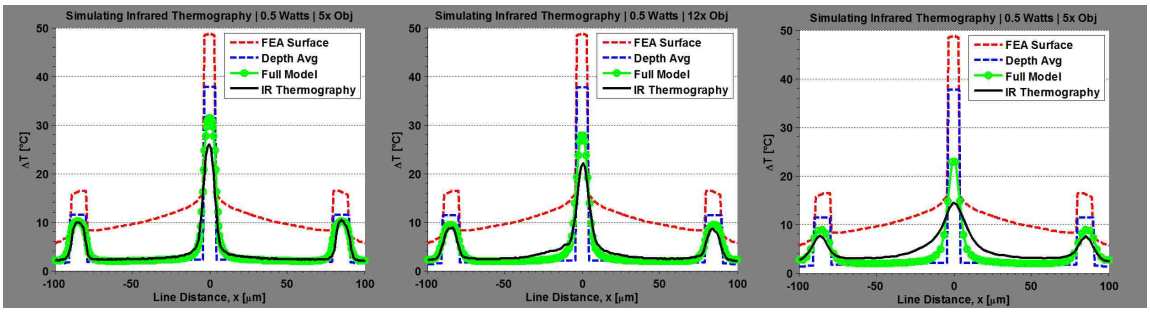


Figure 5.13: FEA surface temperature with full simulation vs measured IR temperature for a power input of 0.5 Watts at various objective magnifications.

As the figures indicate, infrared thermography simulation of the control shows strong resemblance to the measurement. The simulated profiles would likely vary some were the diffraction induced lateral average taken in 2-D as opposed to our

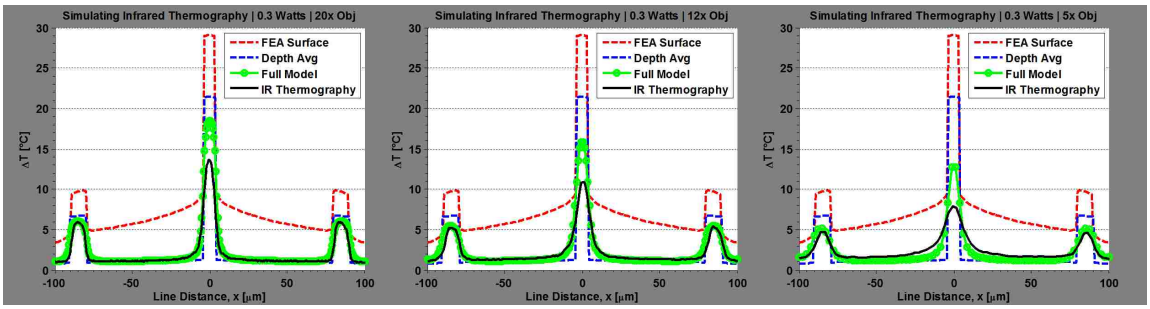


Figure 5.14: FEA surface temperature with full simulation vs measured IR temperature for a power input of 0.3 Watts at various objective magnifications.

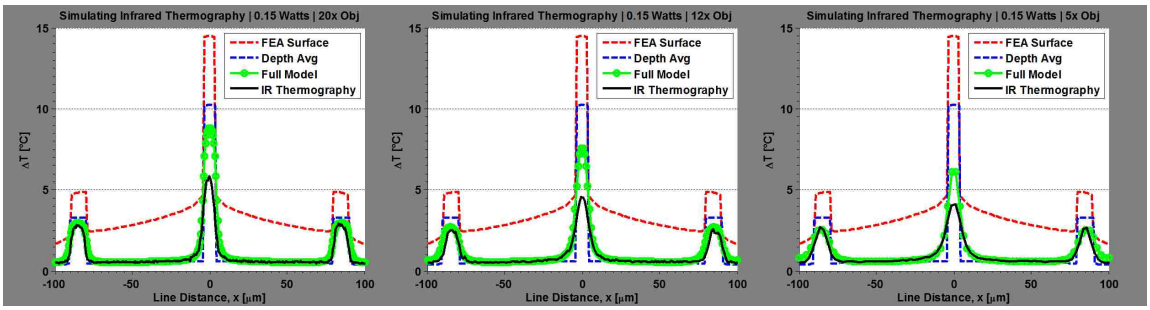


Figure 5.15: FEA surface temperature with full simulation vs measured IR temperature for a power input of 0.15 Watts at various objective magnifications.

line scan. The added dimension would result in the sampling of more non-heater region and therefore reduce peak temperatures where the heater becomes thin. We especially see this over the center heater section as its relatively small width occupies less of the circular sampling spot area. To the same effect, we see a reduction in model accuracy for decreasing magnification due an increasing diffraction sampling spot size, and thus an increase in weight toward the non-heater region temperature in the measurement.

The consistency and reasonable accuracy between each simulation to measurement comparison suggests that our methods are sound, and that both the FEA control model and measurements are valid.

# Chapter 6

# Conclusions and Suggested Future Work

## 6.1 Carbon Based Topside Thermal Solutions

Numerical simulations were used to study the capability of carbon materials as a top-side thermal solution for the management of hot spots in microelectronics. The results indicate that while a micoelectronic device can benifit highly from a topside thermal solution, the use of single and multi-layer graphene as heat spreaders is inadequate, despite possessing high thermal conductivities, which do not make up for their atomically thin dimensions. Instead, a thick heat spreader of moderate conductivity will act as a more efficient conduit for thermal transport, and thus a more effective thermal solution. A thick heat spreader with a high thermal conductivity is ideal, and represents our best case scenario of CVD diamond or HOPG. Perhaps most import however, is the proximity of the spreader to the hot spot, as the spreader becomes completely ineffective when its thermal path becomes to resistive. Adding a topside heat sink in series with a heat spreader is best used as a supplementary

solution, since implementing a heat spreader is less complicated and accounts for the majority of cooling. Still, a heat sink can further promoting hot spot reductions for up to about 15% of additional cooling for the considered simulation parameters, and can have additional substrate cooling effects. Ultimately, this study shows how devices can benefit from a topside thermal solution through significant reductions in maximum temperatures, leading to reduced power limitations, as well as a boost in longevity and efficiency.

## 6.2 IR Thermography Simulations

The work involved in this thesis as well as other aspects of the project that funded this work utilized a fair amount of IR thermography. IR thermography has many benefits over competing techniques, leading to its heavy use in both industry and academics. It is a passive technique that measures naturally emitted infrared light, thus having little influence on the system it is probing. It is capable of capturing large amounts of data very quickly, and does not require any special means of powering the device under test. However it is known that the relatively long wavelength of the leveraged infrared light can introduce large errors into the measurement, which we began witnessing first hand. As we investigated the mechanisms behind these errors to understand them better, we began developing a model to simulate the measurement on known device parameters to compare with measured data. After a number of program iterations, the final model included a transfer matrix methodology which allows for analysis on any number of material layers and accounts for light absorption, reflections, and interference patters. The model could handle wavelength and temperature dependent properties, which were all built on the complex refractive index of each material unless otherwise defined. It can input any temperature profile and create interpolation functions for smooth continuous quadrature numerical

integration, either from an FEA model for validation through an IR measurement, or approximate profiles that scale up with temperature for rough measurement calibration curves.

The model takes device parameters and follows measurement procedures to obtain depth averaged temperatures, which unlike the measurement, account for light diffraction averaging post processing. The assigned diffraction parameters are based on system specific measured characteristics, and despite being accounted for post processing, look to mimic the measured diffraction induced errors fairly well. By combining and comparing FEA simulations, electrical resistance thermometry, IR thermography, and the developed volumetric averaging technique, we were able to arrived at the conclusion that both the FEA control model and volumetric averaging technique are valid to within reason. The valid FEA control model provides confidence in the topside thermal solution simulation results, and the valid volumetric averaging technique opens a door to better general measurement analysis and a new approach to FEA model validation.

## 6.3 Future Work

The carbon based topside thermal solution results offer promising options for hot spot management in microelectronics, and present nice guidelines for future implementation. However the models are idealized and only consider a single isolated active device. It would behoove the study to incorporate a non-idealized thermal interface to the package, and perhaps remove the assumption that the package remains at room temperature. More complex device architectures could also be considered, which might dissipate heat over a larger region, possibly influencing the performance of each topside thermal solution. Specifically, since many devices and device designers may not allow a blanket heat spreader configuration, perhaps the moated

configuration would be more impactful in a less idealized environment. Additionally, experimental investigations of the heat spreader configurations could confirm the findings of the simulations, and remain a future objective.

In regards to simulating IR thermography, a number of areas could be improved and utilized. Within the scope of the presented work, the first improvement I would suggest is to make the light diffraction induced lateral averaging two dimensional instead of the one dimensional analysis described. This would require that depth averages be taken over a large area instead of the one dimensional line over the heater. To make that a reality, a better interface between the FEA model and the MATLAB program would be highly beneficial and could ultimately become a post processing module within FEA software.

# References


[1] E. Pop, V. Varshney, and A. K. Roy, "Thermal properties of graphene: Fundamentals and applications," *MRS Bulletin*, vol. 37, 2012.

[2] A. A. Balandin, "Thermal properties of graphene and nanostructured carbon materials," *Nature Materials*, vol. 10, 2011.

[3] W. Jang, Z. Chen, W. Bao, C. N. Lau, and C. Dames, "Thickness-dependent thermal conductivity of encased graphene and ultrathin graphite," *Nano Letters*, vol. 10, 2010.

[4] A. Sukhadolaua, E. Ivakina, V. Ralchenkob, A. Khomichc, A. Vlasovb, and A. Popovichb, "Thermal conductivity of cvd diamond at elevated temperatures," *Elsevier*, 2005.

[5] P. F. Salazar, S. Kumar, and B. A. Cola, "Nitrogen- and boron-doped carbon nanotube electrodes in a thermo-electrochemical cell," *Journal of The Electrochemical Society*, vol. 159, 2012.

[6] B. A. Cola, X. Xu, T. S. Fisher, M. A. Capano, and P. B. Amama, "Carbon nanotube array thermal interfaces for high-temperature silicon carbide devices," *Nanoscale and Microscale Thermophysical Engineering*, vol. 12, no. 3, 2008.

[7] M. Fujii, X. Zhang, H. Xie, H. Ago, K. Takahashi, T. Ikuta, H. Abe, and

T. Shimizu, "Measuring the thermal conductivity of a single carbon nanotube," *Physical Review Letters*, vol. 95, 2005.

[8] C. Rochford, S. Limmer, S. Howell, T. Beechem, and M. Siegal, "Planarized arrays of aligned, untangled multiwall carbon nanotubes with ohmic back contacts," *Cambridge Journal of Materials Research*, vol. 30, no. 2, 2014.

[9] S. Subrina, D. Kotchetkov, and A. A. Balandin, "Heat removal in silicon-on-insulator integrated circuits with graphene lateral heat spreaders," *IEEE Electron Device Letters*, vol. 30, 2009.

[10] Z. Gao, Y. Zhang, Y. Fu, M. M. Yuen, and J. Liu, "Thermal chemical vapor deposition grown graphene heat spreader for thermal management of hot spots," *Elsevier*, 2013.

[11] Z. Yan, G. Liu, J. M. Khan, and A. A. Balandin, "Graphene quilts for thermal management of high-power gan transistors," *Nature Communications*, 2012.

[12] L. Yu, D. Dai, and S. He, "Graphene-based transparent flexible heat conductor for thermally tuning nanophotonic integrated devices," *Applied Physics Letters*, vol. 105, 2014.

[13] X.-Q. Miao, L.-J. Huang, W.-S. Zhao, and W.-Y. Yin, "Suppressing temperature rise in algan/gan hemt with graphene layers," *Electrical Design of Advanced Packaging and Systems Symposium*.

[14] N. Han, T. V. Cuong, M. Han, B. D. Ryu, S. Chandramohan, J. B. Park, J. H. Kang, Y.-J. Park, K. B. Ko, H. Y. Kim, H. K. Kim, J. H. Ryu, Y. Katharria, C.-J. Choi, and C.-H. Hong, "Improved heat dissipation in gallium nitride light-emitting diodes with embedded graphene oxide pattern," *Nature Communications*, vol. 4, no. 1452, 2013.

[15] CINDAS, "Thermophysical properties of matter database," 2014.

[16] P. E. Hopkins, M. Baraket, E. V. Barnat, T. E. Beechem, S. P. Kearney, J. C. Duda, J. T. Robinson, and S. G. Walton, "Manipulating thermal conductance at metalgraphene contacts via chemical functionalization," *Nano Letters*, vol. 12, 2012.

[17] S. S. Mahajan, G. Subbarayan, and B. G. Sammakia, "Estimating kapitza resistance between si-sio2 interface using molecular dynamics simulations," *IEEE Transactions on Components, Packaging and Manufacturing Technology*, vol. 1, no. 8, 2011.

[18] J. Yang, M. Shen, Y. Yang, W. J. Evans, Z. Wei, W. Chen, A. A. Zinn, Y. Chen, R. Prasher, T. T. Xu, P. Keblinski, and D. Li, "Phonon transport through point contacts between graphitic nanomaterials," *Physical Review Letters*, vol. 112, 2014.

[19] S.-W. Chang, A. K. Nair, and M. J. Buehler, "Geometry and temperature effects of the interfacial thermal conductance in copper and nickelgraphene nanocomposites," *Journal of Physics: Condensed Matter*, vol. 24, 2012.

[20] J. H. Seol and et al., "Two-dimensional phonon transport in supported graphene," *Science*, vol. 328, 2010.

[21] J. Chen, G. Zhang, and B. Li, "Thermal contact resistance across nanoscale silicon dioxide and silicon interface," *AIP*, vol. 112, no. 064319.

[22] B. Gundrum, D. G. Cahill, and R. S. Averback, "Thermal conductance of metal-metal interfaces," *Physical Review B: Condensed Matter and Materials Physics*, vol. 72, no. 24, 2005.

[23] Y. Cengel and A. Ghajar, *Heat and Mass Transfer Fundamentals and Applications*, vol. 4. Mc Graw Hill, 2011.

[24] H. O. McMahon, "Thermal radiation from partially transparent reflecting bodies," *Journal of the Optical Society of America*, vol. 40, no. 6, 1950.

[25] P. J. Timans, "Emissivity of silicon at elevated temperatures," *J. Appl.Phys*, vol. 74, 1993.